Powder Metallurgy Progress, Vol.22 (2022), No.1, p.001-006
http://dx.doi.org/10.2478/pmp-2022-0001

ANNOUNCEMENTS

Professor RNDr. Ján Dusza, DrSc – 70 years jubeeleum

Professor RNDr. Ján Dusza, DrSc. is an internationally known, highly qualified expert in fracture mechanics and in the field of development and complex characterization of advanced ceramic materials at the macro-/micro- and nano-levels both at room and high temperatures. He obtained numerous recognitions and awards for his research activities, including the ESET Science Award and the Alexander von Humboldt Award.

After completing his undergraduate studies in materials physics at ELTE University in Budapest, prof. Dusza started his career at the Institute of Materials Research of the Slovak Academy of Sciences in Kosice as a doctoral student. At IMR SAS he formed as a successful researcher, and later become a head of the Department of Structural Ceramics, deputy director for science, and held several positions in the scientific council of the institute. Currently, he is the head of the Division of Non-metallic Systems and a member of the Administrative Board of IMR SAS at the same time, he is head of the Research Center of Progressive Materials and Technologies for Current and Future Applications – PROMATECH. He has lectured at several universities in Slovakia, Hungary, Austria, and Germany, holds professorships at TU Kosice, and Obuda University Budapest in Hungary, and is an honorary professor at Northwestern Polytechnical University in Xi'an, China. He actively participates in the education of the young scientific generation. So far he has supervised 15 PhDs. students currently have 4 students in doctoral studies. In addition to lectures at universities, he also co-authored several university textbooks. Many of his former PhDs. students continue an active scientific career.

His more than 40 years of continuous scientific and research activity also speaks of the established international cooperation between Slovak scientists and scientists from abroad, especially from the USA, Great Britain, Hungary, Poland, the Czech Republic, and China. At home, he coordinated EU framework program projects, as well as several international and domestic projects (e. g. VEGA, APVV, European Commission 5th – 7th EU framework program, Phare, British Council, Royal Society, BMFT, COST, MNT – ERA, FLAG – ERA, EU Structural Fund Projects in Slovakia, etc.). He was one of the main initiators of the establishment of the NANOSMART Center of Excellence, the Center of

Excellence for Advanced Materials with a nano and submicron structure, and the research center for advanced materials and technologies – PROMATECH. Through his activities, he contributed significantly to building the infrastructure of the IMR SAS.

He participated in the organization of many scientific conferences and seminars, for example, the international conference "Fractography of Advanced Ceramics", dedicated to the fractography of ceramic materials, which is the only one in the given scientific field in Europe.

Despite the already long list of achievements, he is still very active in stimulating new research ideas in cooperation with his doctoral students, postdoctoral fellows, and colleagues from Slovakia and abroad. Last but not least, he popularizes the area of his scientific interest to the general public at many events.

Throughout his scientific career, Professor Ján Dusza focused on the research of new, unexplored ceramic materials. He focused on materials with an excellent combination of resulting properties at both room and high temperatures. To improve the high-temperature properties of composite ceramics, he investigated the effect of adding ceramic nanoparticles to the submicron matrix. During the research, he also came up with the idea of how to improve the mechanical and tribological properties of ceramics by incorporating carbon nanostructures. A significant improvement was achieved mainly in fracture toughness due to strengthening mechanisms. Among the first in the world, he described the influence of the addition of graphene sheets on the microstructure development and fracture toughness of Si_3N_4 + GPLs composites and the role of strengthening mechanisms such as crack deflection, crack branching, and crack bridging during strengthening. Another important area of his research was based on the idea of using nanoindentation, micropillar, and microcantilever test to understand the deformation characteristics of brittle ceramics. The idea of using nanoindentation to characterize individual grains was fully developed during the study of a new type of ceramics – high-entropy carbides. The result was the first publication in the world describing the technological preparation, microstructure, and properties of bulk high entropy carbide. Recently he started research in ceramic and carbon-based nanofibers by electrospinning technology, field-assisted sintering technology (sintering under pressure and electric field), and development of methods for testing mechanical properties at the micro/nano levels using an electron microscope with a focused ion beam. During many years of research work, he led the group at IMR SAS, and thanks to his cooperation with many domestic and international research teams, he achieved the aforementioned remarkable

results.

The Editorial Office and Editorial Advisory Board of Powder Metallurgy Progress wants to congratulate and wish Professor Ján Dusza all the best, many health, and inspiration for his further scientific achievements.

POWDER METALLURGY PROGRESS,

an international open-access journal with 20 years of publishing history announces the

EXTENSION OF THE JOURNAL`S SCOPE

Works from the fields of powder metallurgy, all powder-derived materials - metals, alloys, ceramics, and composites, and basic and applied research of materials science related to mechanical and functional properties, manufacturing, and characterization are always welcomed.

But in 2021 the Scope of the Powder Metallurgy Progress will be extended to:

- materials research such as materials physics, materials chemistry, materials engineering, traditional and advanced powder metallurgy, and materials processing;
- wide range of metal, ceramic and composite materials including metal matrix, ceramic matrix, polymer matrix composites, and hybrid organic-inorganic-metal-ceramic material systems, structural materials, functional materials, biomaterials, porous materials, magnetic electric and multifunctional materials such as magnetic composites, magnetoelectric, magnetocaloric, ferroelectric, piezoelectric, thermoelectric, magneto-optic, magnetostrictive, or high-temperature materials;
- advanced as well as traditional production technology and processing, additive manufacturing, 3D printing, Press and Sinter, HIP, MIM, PIM, Spark Plasma Sintering, Hot Pressing, Microwave Sintering, Plasma Treatment, Slip Casting, Rapid Heating, Ultrafast Sintering, new progressive compaction and processing methods;
- influence of material processing parameters on their microstructure formation and development and structural relations of physical, mechanical, and functional properties of materials focusing but not limited on powder materials;
- special technological processes of PM material with individual-particular-special physical-chemical properties;
- environmental issues of production and application of PM materials;
- industrial processes, management, and quality, (creation of normative) standard method activity, economical analysis, conception (philosophy) and prediction in PM and progressive material processing field;

- production of technological equipment for powder and advanced materials technology.

For more details visit the PMP homepage.

Powder Metallurgy Progress, Vol.22 (2022), No.1, p.007-013
http://dx.doi.org/10.2478/pmp-2022-0002

FRACTURE TOUGHNESS OF CEMENT PASTE ASSESSED WITH MICRO-SCRATCH AND ACOUSTIC EMISSION

Jiří Němeček, Radim Čtvrtlík, Lukáš Václavek, Jiří Němeček

Abstract

Micro-scratch test was used to evaluate the fracture toughness of the main hydration products of ordinary Portland cement paste at the micro-scale. The evaluation was done with the aid of scanning electron microscopy and acoustic emission (AE) signals. Portlandite was found to be the only phase where AE detected elastic waves due to cracking during microindentation and micro-scratch test. Such behavior simplifies phase separation during the evaluation process of the micro-scratch test. The micro-scale fracture toughness results obtained from the tests were found in close agreement with other available experiments and models in the literature.

Keywords: scratch test, acoustic emission, fracture toughness, cement paste, microindentation

INTRODUCTION

Cement paste is a heterogeneous material consisting of several phases at the micrometer scale [1]. Assessing a local fracture of the phases is a challenging task since standard nanoindentation does not give quantitative results due to the inaccessibility of the fracture surface [2]. Thus, another approach producing micro-cantilevers [3] or pillars [4] by focused ion beam (FIB) was proposed. The manufactured specimens are further mechanically tested with a nanoindenter. The method allows tensile/compressive experiments or fracture energy measurement [3,4]. Despite the high reliability of the FIB technique, the manufacturing process is very time-consuming and costly. Thus, the scratch test presents a convenient way for local fracture toughness evaluation [5,6]. The technique was successfully used on many materials e.g. ceramics, polymers, metals [5,6], or cement composites [7], where homogenized fracture toughness consisting of all phases was measured as 0.65±0.01 MPa·m$^{1/2}$. Yet, the properties of individual hydration products were not measured due to the high vertical force (2 N) used during the experiment and smaller forces are necessary

The aim of the work is to disclose local fracture toughness at the level of individual cement paste phases, i.e. at the level of micrometers. Due to cement heterogeneity, the mechanical response is not sufficient for the reliable separation of individual phase properties. Therefore, the scratch test needs to be supported by other techniques such as scanning electron microscopy (SEM) using ex-post separation or acoustic emission (AE) measured simultaneously with nanoindentation testing.

This work was presented at the conference Local Mechanical Properties 2022 held in Kosice, Slovakia on May 11-13, 2022.

Jiří Němeček, Jiří Němeček: Department of Mechanics, Faculty of Civil Engineering, Czech Technical University in Prague, Thákurova 7, 166 29 Prague 6, Czech Republic

Radim Čtvrtlík, Lukáš Václavek: Institute of Physics of the Czech Academy of Sciences, Joint Laboratory of Optics of Palacký University and Institute of Physics AS CR, 17. Listopadu 50a, 772 07, Olomouc, Czech Republic

Lukáš Václavek: Palacký University in Olomouc, Faculty of Science, Joint Laboratory of Optics of Palacký University and Institute of Physics AS CR, 17. Listopadu 12, 771 46, Olomouc, Czech Republic

The AE is a non-destructive method that detects elastic waves emitted during the phase cracking [8] and can be directly synchronized with the force-depth-time results. It provides information otherwise unavailable by mechanical tests [9].

MATERIALS AND METHODS

Sample preparation

A cement paste sample was prepared from ordinary Portland cement CEMI-42.R (Českomoravský cement, Czech Republic). A fresh paste with a water-to-cement ratio of 0.4 was cast into cylindrical molds with a diameter of 27 mm and a height of 70 mm. The samples were demolded after 24 hours and stored in the water for 4 months to achieve a high degree of hydration. After the curing period, the samples were cut by a precise diamond saw into 6 mm thick slices. The slices were then put into the oven for 24 hours. After that, the slices were finely polished with silicon carbide papers according to the procedure described in [10]. The polished samples were then put into the ultrasonic bath to remove all free particles from the samples.

Typical microstructure at the level of cement paste (below 100 μm) is shown in the back-scattered electron (BSE) image in Fig. 1. The microstructure is highly heterogenous, created mainly by outer product (OP) and inner product (IP), which are rich Calcium-Silicate-Hydrate (C-S-H) gel mixed with other hydrates. Also, with less represented phases, which are crystalline Calcium Hydroxide - Portlandite (CH), residual clinker (C), and capillary porosity.

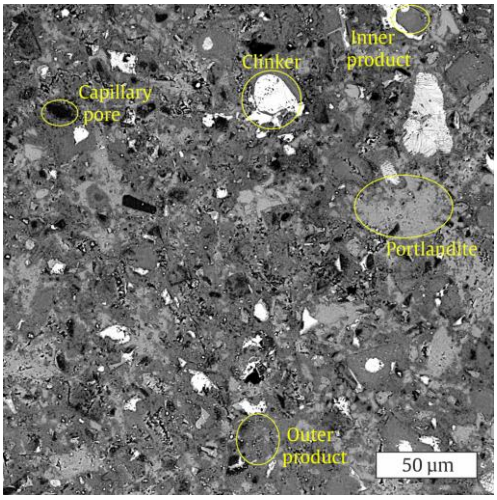

Fig. 1. SEM-BSE image of typical cement paste microstructure.

Microindentation

The microindentation was performed with the NanoTest Vantage system (Micro Materials Ltd.) equipped with a spherical diamond tip of 10 μm radius. A grid of 5 × 10 indents with a separation of 40 μm was performed with a trapezoidal loading diagram. In the first segment, the sample was linearly loaded with a loading rate of 5 mN/s (10 seconds) up to the maximum force of 50 mN. During the second segment, the force was held for 20 seconds. Lastly, the sample was linearly unloaded for 10 seconds.

Scratch test

The scratch tests with a total length of 450 μm were performed with the same tip and nanoindenter as microindentation. The load function of the scratch test consists of three segments. In the first segment (0-50 μm), the sample was loaded with a contact vertical force, F_N, of 0.05 mN. In the second segment (50-200 μm), the vertical force was linearly increased up to the maximum force of 50 mN. In the third segment (200-450 μm), the maximum force was kept constant. In the horizontal direction, the tip velocity of 10 μm/s was prescribed. The penetration depth, d, and horizontal force, F_T, were recorded during the scratch test. Since the total scratch length is relatively large, the measured penetration depth was corrected by the inclination of the sample measured by scratch pre-scan with a contact force of 0.05 mN. In total, 20 scratch tests were performed.

The fracture toughness, K_c, was evaluated from scratch test by the relationship between the horizontal force and the tip geometry derived by Akono and Ulm [5,6] as

$$K_c = F_T / (2p(d)A(d))^{1/2}, \quad (1)$$

where $A(d)$ is the horizontal load-bearing contact area, and $p(d)$ is the horizontal contact perimeter. The function $T(d) = 2p(d)A(d)$ represents the tip geometry which is calibrated according to the function

$$T(d) = R^3 \cdot [\alpha(d/R)^3 + \beta(d/R)^3 + \gamma(d/R)], \alpha \geq 0, \beta \geq 0, \gamma \geq 0, \quad (2)$$

where α, β, γ are the fitting coefficient of the function, and R is the radius of the spherical tip. The coefficients were calibrated as $\alpha = 298.1$, $\beta = 0$, $\gamma = 0$ on the fused silica glass with a known value of $K_c = 0.80$ MPa·m$^{1/2}$.

Acoustic emission

The acoustic emission signal was continuously recorded during microindentation and scratch tests by the ZEDO system (Dakel). A high dynamic range and sampling frequency of 10 MHz enable the measurement of very weak and strong AE events at the micro-second scale. The low-temperature wax fixed the sample on the AE holder with an inbuild pre-amplifier. The data were measured in the frequency range of 100 – 1500 kHz.

To quantify AE activity, the count system approach was used. Every time the signal crosses the predefined threshold set to 6 μV the hit is counted. The hit corresponds to phase cracking or phase transformation during the mechanical test [9].

EXPERIMENTAL RESULTS AND DISCUSSION

Results of microindentation

The results of microindentation were separated into four mechanical phases: inner product (IP), outer product (OP), Portlandite (CH), and residual clinker (C), Figure 1. However, some interaction was possible between the phases due to a relatively large indentation force of 50 mN used. Thus, only indents with one dominant phase, recognized with the aid of SEM images (Fig. 2), were taken into account in further analysis. Based on the SEM observations of the visible indents, cracks were created around all indents. Despite direct crack observation, AE hits were acquired only for the Portlandite phase during the loading period, see Fig. 3. The AE hits were accompanied by pop-ins visible on both force-displacement (Fig. 4(a)) and displacement-time curves (Fig. 3(a)). The pop-ins correspond exactly to the location of AE hits. It suggests that AE recorded discontinuities activation

due to slipping planes of the Portlandite crystal. From the much lower AE signal, it may be deduced that the deformation mechanisms of OP and IP are different. The cracks are created after exceeding the tensile strength of the material during the loading period. In this case, the AE signal was probably dampened in highly disordered and amorphous cement paste due to the large thickness of the samples (6 mm).

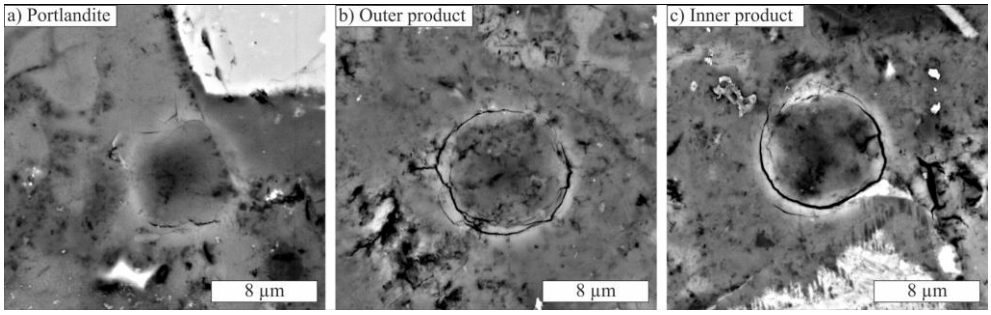

Fig. 2. SEM-BSE images of the indents imprint in (a) Portlandite, (b) Outer product, (c) Inner product.

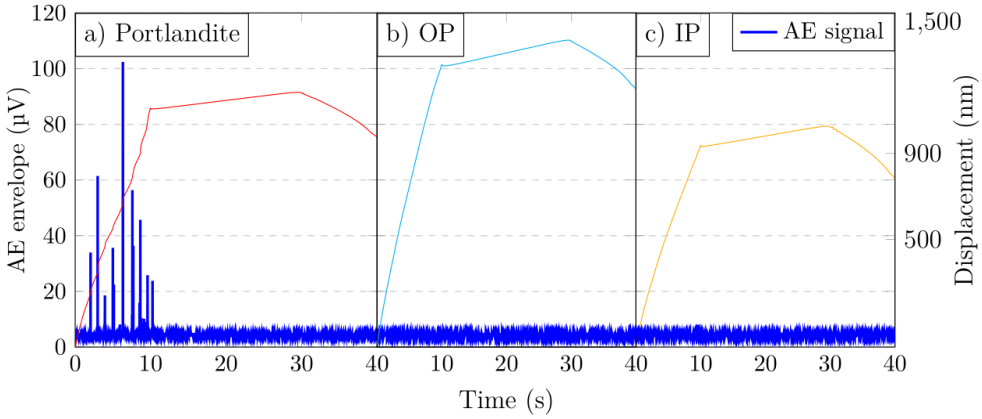

Fig. 3. Displacement-time curves with recorded AE signal of (a) Portlandite, (b) Outer product, (c) Inner product.

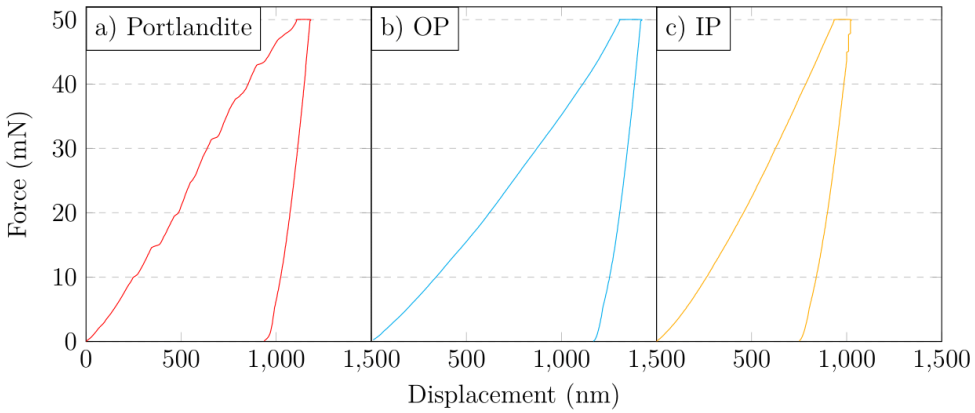

Fig. 4. Typical force-displacement curves of (a) Portlandite, (b) Outer product, (c) Inner product.

Results of scratch tests

The fracture toughness, K_c, was evaluated from lateral force measurements and using Eq. (1). The toughness varied over a wide range of values from 0.05 to 2.1 MPa·m$^{1/2}$. The separation of mechanical response was done in the same way as for microindentation into four mechanical phases. Large pores visible on the SEM-BSE images (Fig. 5a) were excluded from the analysis. The calculation of the mean K_c value for a given phase was done manually between two points and is highlighted in Fig. 5(b). During the separation process, two factors were considered: first SEM-BSE images (Fig. 5(a)), providing a very good overview of phase location in the scratch line, and second, the AE signal (Fig. 5(c)) used as the Portlandite cracking process indicator. Since Portlandite, similarly as in microindentation, was the only phase where AE hit was observed. In some rare cases, AE hit was observed in another phase, e.g. at scratch distances 130 µm and 170 µm (Fig. 5(c)) suggesting a small amount of CH intermixed with OP was scratched. The summary of fracture toughness results is shown in Tab. 1. The K_c value of the most frequent phase OP was evaluated as 0.34±0.03 MPa·m$^{1/2}$. The obtained value is in close agreement with a molecular dynamic simulation of C-S-H gel, where fracture toughness was calculated as 0.37±0.01 MPa·m$^{1/2}$ [11]. Moreover, very good agreement was found with the micro-beam bending experiment where K_c = 0.33±0.06 MPa·m$^{1/2}$ [3].

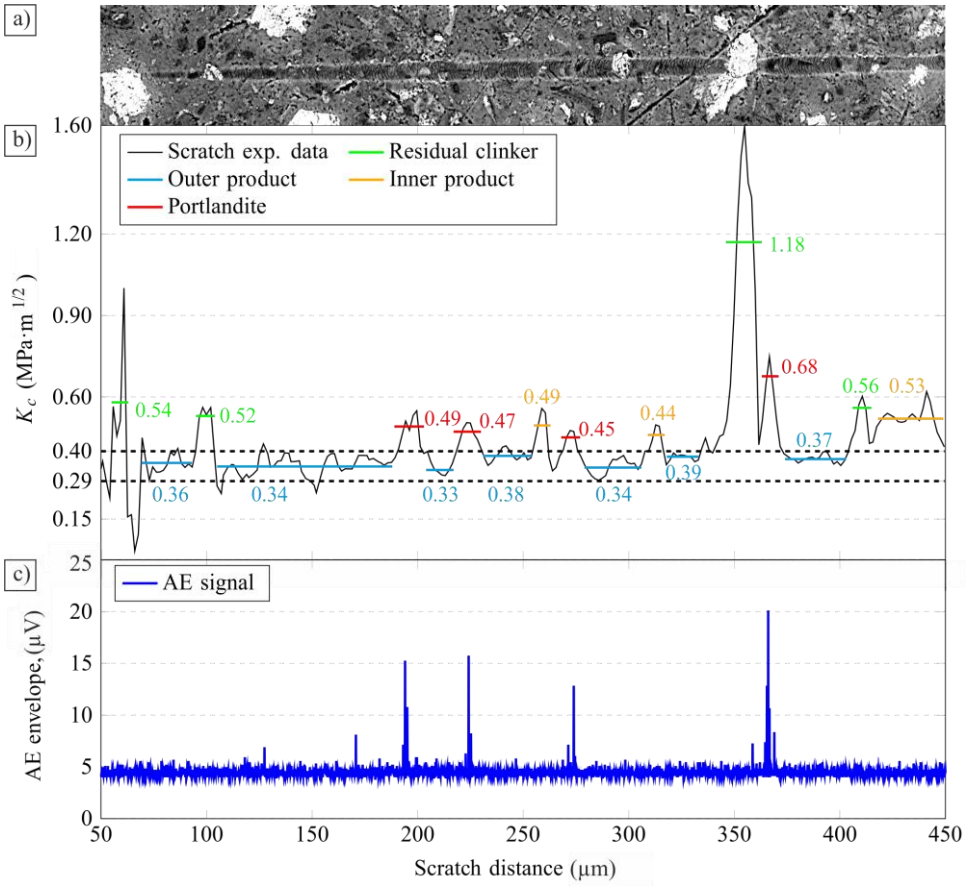

Fig. 5. a) SEM-BSE image of the scratch line; b) fracture toughness calculated from the scratch test with the highlighted mean values of phases; c) record of AE signal.

Tab. 1. Summary of cement paste fracture toughness obtained at micro-scale.

Test method	K_c (MPa·m$^{1/2}$)				Reference
	OP	IP	CH	C	
Scratch test	0.34±0.03	0.49±0.04	0.47±0.05	0.84±0.31	this study
Micro-beam bending	0.33±0.06	0.81±0.08	0.88±0.28	--	[3]
Micro-pillar compression	--	0.67	--	--	[4]
Molecular dynamic	0.37±0.01	--	--	--	[11]

Obtained fracture toughness of IP (K_c = 0.49±0.04 MPa·m$^{1/2}$) and CH (K_c = 0.47±0.05 MPa·m$^{1/2}$) were higher than in OP. However, lower values, as compared to the micro-beam experiment, was found, see Tab. 1. The reason lies in the phase interaction and intermixing in the microstructure and the given indentation volume since the phase volume of IP and CH is relatively small compared to the scratch dimension. The highest fracture toughness value of all the phases was that of residual clinker with K_c = 0.84±0.31 MPa·m$^{1/2}$. This mean value corresponds to clinker particles of all dimensions appearing in the scratch line. If a large clinker particle with dimensions over 20 μm was scratched, the

values increased to 1.23-2.12 MPa·m$^{1/2}$. It must be noted that the clinker is composed of several mineralogically different constituents, perhaps characterized by very different fracture toughness.

CONCLUSIONS

The paper shows the application micro-scratching technique coupled with acoustic emission signal in micro-mechanical experiments of cement paste. The acoustic emission very reliably detects the presence of a crystalline phase called Portlandite in a measured volume during microindentation and micro-scratch test, which was confirmed also by SEM-BSE images. Despite clearly visible cracks in SEM images of other phases (outer product, inner product, residual clinker), the acoustic emission signal did not recognize any cracking. The reason is, perhaps, given by the sample thickness (6 mm) and the highly amorphous and disordered nature of the tested material which caused damping of the AE signal.

The micro-scratch experiment was used for the evaluation of the fracture toughness of cement paste constituents at the micro-scale (below ~100 μm). The phase separation was done with the aid of SEM or AE signal, which significantly simplified and refined the process. The fracture toughness of the most frequent phase, the outer product (K_c = 0.34±0.03 MPa·m$^{1/2}$), was found in very good agreement with other available experiments [3,4] and models [11]. Smaller fracture toughness of the other hydration products was obtained compared to other techniques (Tab. 1) due to large scratch dimensions and inevitable phase interactions.

ACKNOWLEDGMENT

Financial support of the Czech Science Foundation (project 21-11965S) and the Grant Agency of the Czech Technical University in Prague (SGS22/088/OHK1/2T/11) are gratefully acknowledged. The authors also gratefully acknowledge the support by the Operational Program Research, Development and Education, project CZ.02.1.01/0.0/0.0/16_019/0000754 of the Ministry of Education, Youth and Sports of the Czech Republic.

REFERENCES

[1] Taylor, H.F.W.: Cement chemistry, second edition, 2013.
[2] Němeček, J., Hrbek, V., Polívka, A., Jäger, A.: Framcos 9, 2016, p. 11.
[3] Němeček, J., Králík, V., Šmilauer, V., Polívka, A., Jäger, A.: Cem. Con. Comp., vol. 73, 2016, p. 164.
[4] Shahrin, R., Bobko, C.: Cem. Con. Res., vol. 125, 2019, p. 105863.
[5] Akono, A.T., Randall, N.X., Ulm, F.-J.: J. Mat. Res., vol. 27, 2012, p. 485.
[6] Akono, A.T., Ulm, F.-J.: Wear, vol. 60, 2012, p. 379.
[7] Akono, A.T.: J. Mat. Science, vol. 55, 2020, p. 11106.
[8] Tomaštík, J., Čtvrtlík, R., Dráb, M., Maňák, J.: Coatings, vol. 8, 2018, p. 196.
[9] Čtvrtlík, R., Tomaštík, J., Václavek, L., Beake, Harris, A.J., Martin, A.S., Hanák, M., Abrhám, P.: J. Min. Metals & Mat. Soc., vol. 71, 2019, p. 3358.
[10] Němeček, J., Lukeš, J., Němeček, J.: Mat. Today Commun., vol. 23, 2020, p. 100806.
[11] Bauchy, M., Laubie, H., Qomi, M.A., Hoover, C., Ulm F.-J., Pellenq, R.-M.: J. Non-Cryst. Solids, vol. 419, 2015, p. 58.

sciendo
Powder Metallurgy Progress, Vol.22 (2022), No.1, p.014-024
http://dx.doi.org/10.2478/pmp-2022-0003

EVALUATION OF RESIDUAL STRESS AND TENSILE PROPERTIES OF RAILWAY AXLE USING INSTRUMENTED INDENTATION METHOD.

Daniel Bartoněk, Martin Négyesi and Bohumír Strnadel

Abstract
This paper deals with the characterization of residual stresses of the railway axle made of EA4T steel using the instrumented indentation technique (IIT). Additionally, tensile properties were also evaluated by using IIT. Moreover, the hole drilling method was carried out to measure the residual stress. Multiple comparison tests between conventional methods and IIT were carried out. The obtained results were also discussed against the literature data. Results of the residual stress assessed by IIT and the hole drilling follow the same trend and are in acceptable agreement. The tensile data obtained by IIT were as follows: YS ≥ 420 MPa and UTS ∈ ⟨650-800⟩MPa which is in satisfactory agreement with the results of standardized tensile tests.
Keywords: residual stress, tensile properties, instrumented indentation method, EA4T steel, railway axle, advanced indentation system

INTRODUCTION

Railway axles are one of the most crucial parts which support railway vehicles. A failure would have serious consequences and a failsafe system cannot be used as a backup; it must be designed to be reliable. To ensure a longer lifespan proper maintenance is important as well as evaluating mechanical properties and residual stress. This paper deals with evaluating the residual stress and tensile properties with the indentation method.
Since materials degrade over time and especially crack generation and propagation can lead to a component failure before its life expectancy, it is advised to test industrial facilities in service during operation as well as before use. Most conventional methods are destructive, making them unsuitable for field inspection, meaning non-destructive methods must be introduced. During the collection of specimens, damage to the machine can be caused or stress relief can be caused due to specimen extraction so the specimen can have different mechanical properties from the original site structure meaning they cannot be used as in-service tests. With the introduction of automated indentation systems quasi-non-destructive test methods were introduced [1].

The instrumented indentation technique can evaluate not only hardness but also tensile characteristics. In many components, residual stresses are the results of thermal mismatch or thermal/mechanical processing during their manufacturing and can be purposively introduced in parts to affect their mechanical properties especially to enhance resistance against crack propagation. Hence for correct estimation of the remaining lifespan of the railway axle, it is needed to estimate residual stresses and mechanical properties such as the yield stress (YS) and the ultimate tensile strength (UTS) [1,2,3].

This work was presented at the conference Local Mechanical Properties 2022 held in Kosice, Slovakia on May 11-13, 2022.
Daniel Bartoněk, Martin Négyesi, Bohumír Strnadel: VSB Technical University of Ostrava, Centre for Advanced Innovation Technologies

There are many ways to measure and evaluate the residual stress such as a hole drilling method, a ring core method, a crack compliance method, various diffraction methods, and ultrasonic or magnetic methods [4,5].

This paper deals with the measurement of tensile properties and residual stresses on the radial segment of the railway axle employing instrumented indentation testing (IIT). Furthermore, the residual stress was also evaluated using the hole-drilling method. The results of the IIT were compared to the results of conventional experimental techniques, such as tensile testing and hole drilling. The main objective of this study is to test the reliability of the IIT and validate the results of the IIT.

Nomenclature

Symbol	**Designation**	**unit**
A_c	The projected area of the contact surface between the indenter and the tested sample	mm^2
A_c^T	True contact area	mm^2
A_c^0	Actual contact area	mm^2
a_c	Contact radius	mm
a,b, c	Correlated constants	-
E_{IT}	Indentation modulus (Young's modulus)	N/mm^2
F_{max}	Maximum test force	N
h_d	Elastic deflection depth	mm
h_c	Contact depth of the indenter with the test piece at F_{max}	mm
h_{max}	Maximal indentation depth	mm
h_{pile}	Height of plastic pile up	mm
K	Strength coefficient	-
L_0	Indentation load	N
L_T	Tensile load	N
P_{max}	Maximum load	N
R	Radius of indenter	mm
S	Stiffness	N/mm
α	Proportional constant	-
γ	The half angle between the indenter and material	°
ε	Constant of the shape of the indenter	
ε_T	True strain	-
ε_u	True uniform strain	-
ε_v	Yield strain	-
n_{IT}	Indentation work hardening exponent	-
σ	Tensile strength	N/mm^2
σ_{res}	Surface residual stress	N/mm^2
σ_T	True stress	N/mm^2
σ_{uIT}	Indentation tensile strength	N/mm^2
σ_{yIT}	Indentation yield strength	N/mm^2
ψ	Plastic constraint factor	-

Note N/mm^2 = 1 MPa

THEORETICAL BACKGROUND

Tensile properties evaluation

To be able to measure with indentation methods it is needed to convert indentation load to tensile properties and stress with the corresponding contact area. While in light microscopy area is calculated by observation under the microscope in instrumented indentation testing (IIT) area is calculated from shape of the indenter and the depth of the indent. When testing even if the material is considered not to be elastic material the response always includes elastic deflection and plastic response such as pile-up and sink-in of material. Those factors result in a difference in indentation depth and real contact depth. In the past Oliver-Pharr equation was widely used for contact mechanics (Hertz law) (1).

$$h_d = \varepsilon \frac{P_{max}}{S} \tag{1}$$

Where P_{max} is the maximum load, S is contact stiffness, and ε is the constant of the shape of the indenter (0.75 for spherical indenter). Later the equation was changed [6] to (2)

$$\frac{h_{pile}}{h_c} = f\left(n_{IT}, \frac{h_{max}}{R}\right) \tag{2}$$

Where h_c is contact depth, h_{max} is maximal indentation depth and h_{pile} is the height of plastic pile up, R is the radius of the indenter and n is strain hardening exponent. Afterward using Tabor's relations, the indentation load can be expressed by representative stress σ and mean pressure p_m [7]. Solving multiple equations derived by Kwon, Lee, Kim, Kim, and Choi in 2005 [8] and later followed by Kwon, Kim, Kim, Kim, and Song in 2011 [9] we get to the Eq. (3).

$$\varepsilon_T = \left(\frac{\alpha}{\sqrt{1-\left(\frac{a_c}{R}\right)^2}}\right)\left(\frac{a_c}{R}\right) = \alpha \tan\gamma \tag{3}$$

Where $\varepsilon_T$and α are representative strain and proportional constant. Stress is then defined by the following equation

$$\sigma_T = \frac{1}{\psi}\frac{F_{max}}{A_c} \tag{4}$$

F_{max} is the maximum test force, A_c is the projected area of the contact of the indenter at distance h_c correlated to h_{pile} and h_c from the tip, and A_c is calculated from (5) [10]:

$$A_C = \pi(2Rh_c - h_c^2) \tag{5}$$

For steels, it is then sufficient to use the constitutive Eq. (6) for power-law hardening materials and (7) for linear hardening materials to fit the stress-strain dependence. σ_T is true stress and a, and b are correlated constants. K is Strength coefficient and ε_T is true strain [10]:

$$\sigma_T = K\varepsilon_T^n \tag{6}$$

$$\sigma_T = a + b\varepsilon_T \tag{7}$$

Afterward, it is needed to determine yield strength as the intercept point of the elastic line and plastic curve (8) where E_{IT} is the indentation modulus (Young's modulus), and K is the strength coefficient. E_{IT} is determined from the unloading part of the indentation curve.

$$K\varepsilon_T^{n_{IT}}{}_y = E_{IT}(\varepsilon_y - 0{,}002) \tag{8}$$

The tensile strength is determined by the instability in tension:

$$\frac{d\sigma}{d\varepsilon} = \sigma \tag{9}$$

When combining the Eqs. (6) and (9) we get $\varepsilon_u = c \cdot n_{IT}$, c is the correlated constant, and n is the strain hardening exponent. With Eqs. (2-9) we can calculate tensile properties $\sigma_{y,IT}$, $\sigma_{u,IT}$, n_{IT}, E_{IT} [8,11].

Residual stress evaluation

The fundamentals of evaluating residual stress with the IIT are based on the comparison of the reference place which is stress-free with the target point of interest with measured residual stress. The residual stress shifts the indentation load-depth curve depending on the state of the material. If the material is under tensile residual stress the indenter penetrates deeper into the material than in a stress-free state and likewise, material under compressive residual stress is penetrated less by the indenter. This is shown in Fig. 1.

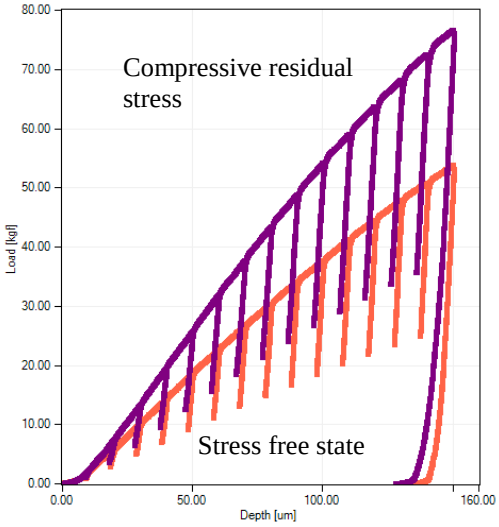

Fig. 1. Comparison of indentation curves in a stress-free state and with residual stress

Since in practice depth is used as constant, to reach the same depth load will be greater/lesser than in a stress-free state depending on residual stress. Assuming the surface residual stress is in equibiaxial tensile state ($\sigma_{res,x}=\sigma_{res,y}=\sigma_{res}$, $\sigma_{res,z}=0$) and by removing hydrostatic stress we get to Eq. 10 [6] where A_C^T is contact area and L_0-L_T is the load shift due to tensile stress:

$$\sigma_{res} = \frac{3(L_0 - L_T)}{2A_C^T} \tag{10}$$

In case that the stress is not completely equibiaxial influence of biaxial stress has to be taken into consideration and ratio p =($\sigma_{res,x}/\sigma_{res,y}$) has to be introduced (11):

$$\sigma_{res} = \frac{3(L_0 - L_T)}{(1+p)A_C^T} \tag{11}$$

However, presented theoretical models deal only with the magnitude of the average stress meaning we do not get any data about the direction or magnitudes of individual components of the stress [5,6,11].

EXPERIMENTAL

Material

The material under study is a radial segment of the railway axle. The dimensions are as follows, the diameter is 18 cm and the segment thickness is 3cm. The surface had been ground up to 2400 grit sandpaper. Chemical analysis of the railway axle has been performed and it was confirmed that the tested material was steel EA4T (25CrMo4). The chemical composition is shown in Tab. 1.[12].

Tab. 1. Chemical composition of the EA4T steel

C [wt %]	Mn [wt %]	Si [wt %]	P [wt %]	S [wt %]	Cr [wt %]	Ni [wt %]	Mo [wt %]
0.0038	0.00489	0.00077	2E-04	3E-04	0.00887	0.00081	0.00145
Cu [%]	Ti [wt %]	Co [wt %]	Pb [wt %]	V [wt %]	W [wt %]	Al [wt %]	Nb [wt %]
0,00006	<0.001	<0.001	<0.001	4E-04	0.0005	0.00011	<0.001

Tensile properties tests

IIT was performed by AIS 3000HD made by Frontics Co., Ltd. The AIS3000HD attached to the railway axle segment via the sample holder is shown in Fig. 2. Every test consists of 15 loading and unloading cycles to a max depth of 150 μm as is shown in

Fig. 3. Tests are performed by spherical indenter from tungsten carbide with a radius of 500μm. The unload ratio is 50%. Multiple tests were performed from the center to the outer surface of the tested axle. However, due to the loading limit of the AIS 3000HD, it was not possible to get precise data in the outer induction hardened layer.

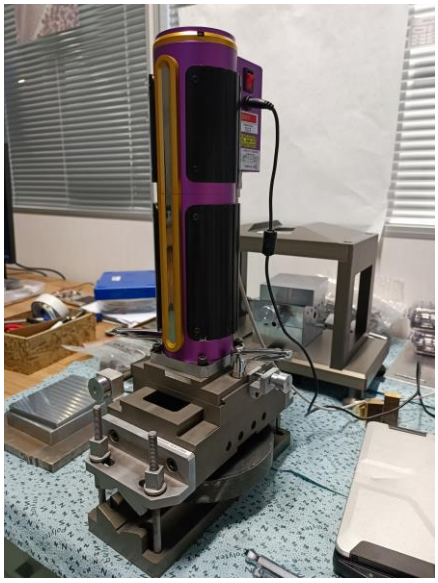

Fig. 2. AIS3000HD with railway axle segment

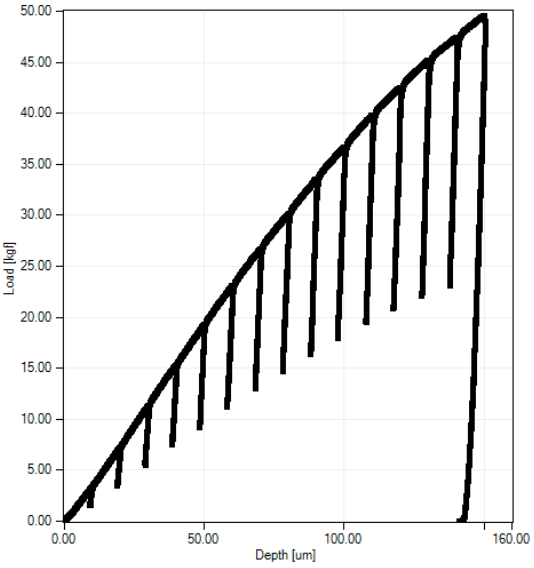

Fig. 3. Load-displacement curve of the tensile test by IIT

Residual stress measurement

IIT was performed with AIS 3000HD. Two sets of tests must be performed for each series. One set is with a spherical indenter and the second set is with a Vickers indenter. Both tests have reference indents in the material without any residual stress and then target spots of interest. The spherical indenter is visible in Fig. 4. Both reference tests consist of 15 loading and unloading cycles with partial unloading with an unloading ratio of 50%. The same goes for target tests with spherical indenter. Unlike the rest of the tests, Vickers target has a single loading cycle to max depth with consequent unloading. With Vickers indenter, the controlling parameter is max load. Using Eqs. (10-11) residual stress is then calculated.

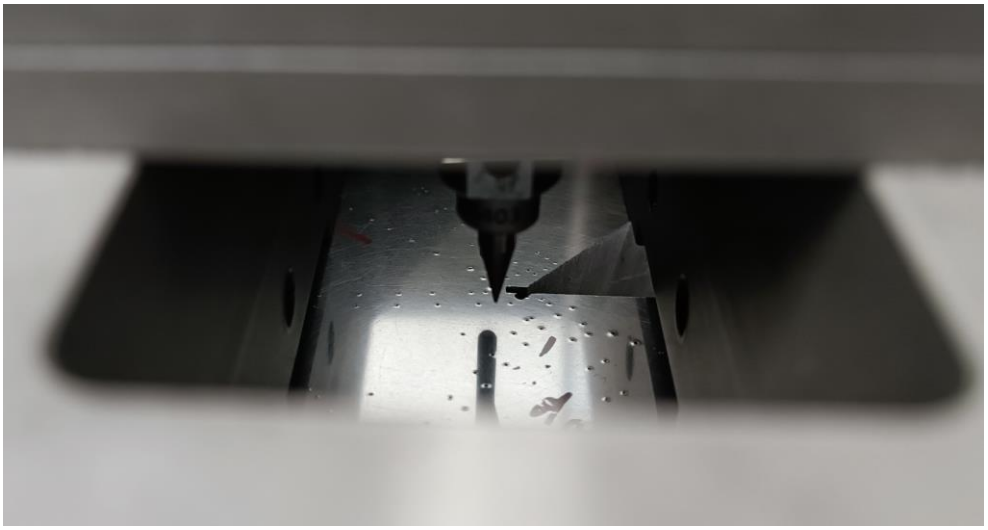

Fig. 4. Spherical indentor of AIS3000HD and visible indents of tests

Hole drilling

Residual stress evaluation by hole drilling method was performed using MTS3000 – RESTAN by SINT technology. First, the surface of the tested specimen was ground. Points of measurement were in distances of 35 mm and 47 mm from the center of the axle. Then strain rosettes were soldered to the tested place and the measuring apparatus was fixed to the axle. The high-speed drill moved down to 2 mm with 0,05 mm increments. For each drilling step, strains created by relaxation were acquired and used to calculate residual stress.

RESULTS AND DISCUSSION

Tensile properties

The reason for the partial unloading is twofold. Firstly, using each unloading cycle is intended to estimate contact radius, F_{max}, h_{max}, and S, and secondly, by partially unloading during the test we relieve elastic deformation, so we get more accurate results of tensile properties. Each test gives us a stress-strain curve depicted in Fig. 5.

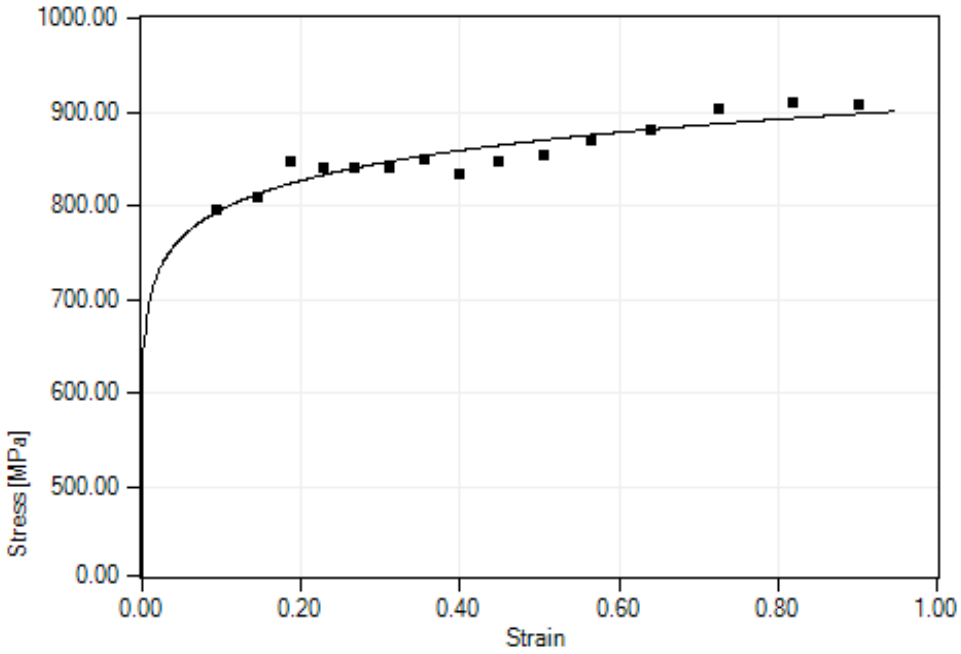

Fig. 5. True stress-strain curve of indentation test performed on AIS 3000HD used for calculations of YS and UTS

Every point in the diagram is one cycle of the tensile test and it gives us values of coefficients, load, and depth by which using Eqs. (5-8) yield strength (YS) and ultimate tensile strength (UTS) are calculated. The measured values are engineering values. 24 tests were performed in 3 rows of 8 and the results are summarized in Tab. 2.

Tab. 2. Results of the tensile tests

No. Of test	1	2	3	4	5	6	7	8
YS [MPa]	597	623	648	591	619	589	665	635
UTS [MPa]	711	782	733	693	748	724	759	733
No. Of test	9	10	11	12	13	14	15	16
YS [MPa]	607	635	614	595	618	650	626	630
UTS [MPa]	707	803	701	698	734	728	710	722
No. Of test	17	18	19	20	21	22	23	24
YS [MPa]	653	615	642	647	620	626	645	389
UTS [MPa]	751	699	727	731	729	764	751	756

The results of tests were discussed against the literature data. The standard EN 13261 [12] sets properties of the EA4T steel in the following way: $YS \geq 420\ MPa$ and $UTS \in \langle 650 - 800 \rangle$. As is visible in Tab. 2. YS as well as UTS are in satisfactory

agreement with the standard values. The values of YS and UTS are plotted in Fig. 6 as functions of the distance from the axle center. The values are independent of the radial distance.

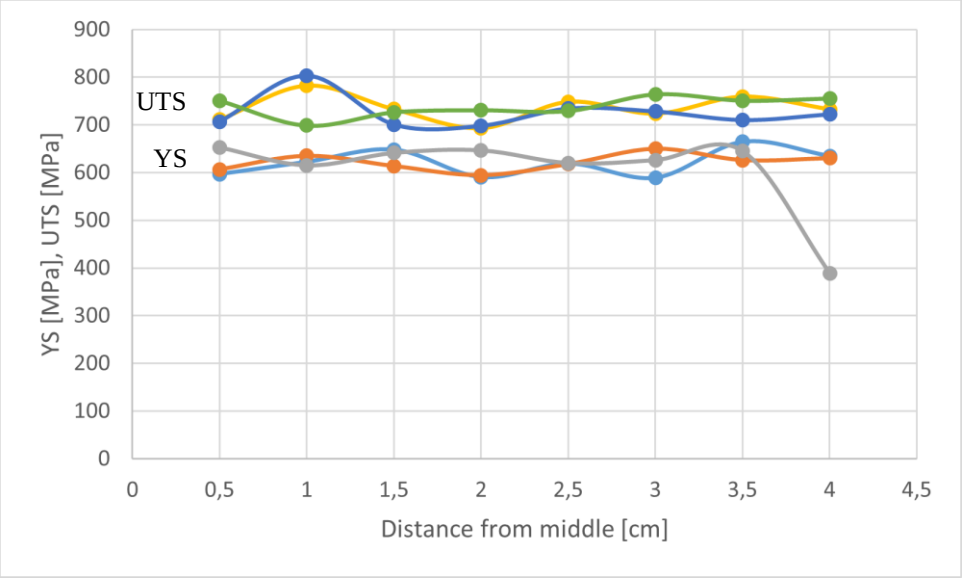

Fig. 6. YS and UTS measured by IIT measured from the middle to the outer surface of the axle

Residual stress

Multiple tests by indentation methods were performed and two tests by drilling method were carried out for comparison. Sets of tests by IIT were performed from the center of an axle to the outer surface. In the inner part of the axle, it was possible to get accurate results, however, in the outer induction hardened layer the results were incorrect due to the loading limit of indentation equipment.

Two tests by drilling method were performed in 35 mm and 47 mm from the middle of the railway axle. The acquired values are presented in Fig. 7 and compared to the results of IIT tests positioned at the same distance from the center of the axle segment. The results are in very good agreement at point 35mm from the middle. The results of the second test by drilling method differ a lot from the first drilling test and tests done by the IIT. The mean values differ considerably. A mean value of 274 MPa was assessed by IIT and a mean value of 115 MPa was determined by the hole drilling.

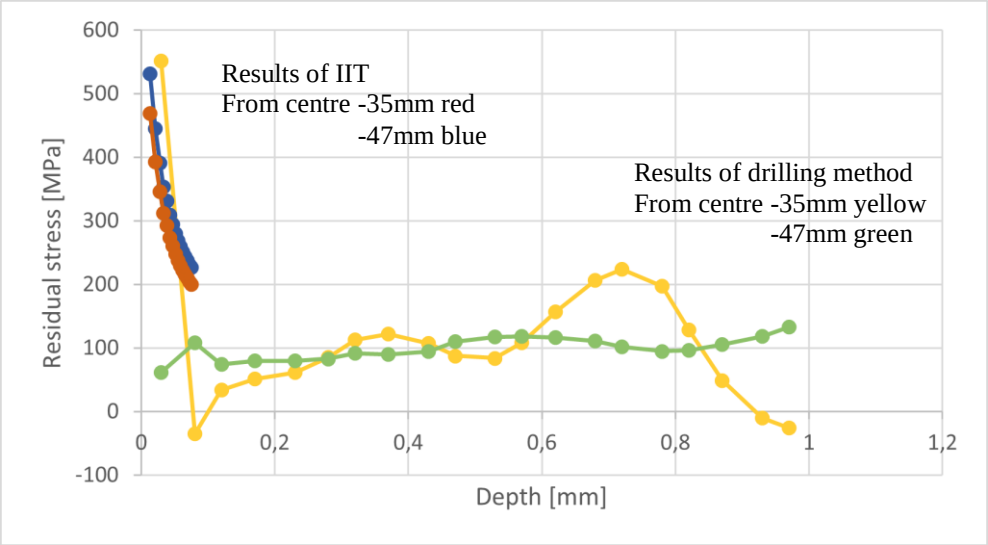

Fig. 7. Residual stress measured by IIT and the drilling method as a function of the depth of measurement.

SUMMARY AND CONCLUSIONS

The possibility of measuring tensile properties and residual stress on the radial segment of the railway axle with instrumented indentation testing was studied.

Multiple tests of tensile properties were performed and as the results were in satisfactory agreement with the standard values, it was shown that IIT is a viable technology for measuring tensile properties.

Series tests of residual stress measurement by IIT were performed and compared to the results of the conventional drilling method. The mean value of the results differs a lot. The hole drilling method results are from a higher depth which influences the mean value by a high margin. However, in the same depth, the results of IIT and hole drilling follow the same trend and are in satisfactory agreement. The results further suggest that surface residual stress can differ by a high margin. IIT has a higher limit in the maximum depth compared to hole drilling. That is why the results may differ substantially.

The results of IIT could not be evaluated in the induction hardened layer of the axle, because the hardness of the material was too high in that area, and consequently, the limit load of AIS3000HD was reached. Further testing by IIT needs to be carried out in this region to find the right parameters.

ACKNOWLEDGMENT

This work was supported by the Doctoral grant competition VŠB TU-Ostrava, reg. no. CZ.02.2.69/0.0/0.0/19_073/0016945 within the Operational Programme Research, Development and Education, under project DGS/INDIVIDUAL/2020-005 " Evaluation of hardness, residual stress, and tensile properties on metallic parts of industrial facilities using Advanced Indentantion System (AIS)".

REFERENCES

[1] Choi, M.J., Lee, K.W., Kim, J.Y., Kim, K.H., Kwon, D.: In Application of instrumented indentation technique to estimate strength and residual stress. 10th Symposium on Recent Advancements in the Theory and Practice of Hardness Measurement 2007, HARDMEKO 2007.
[2] Okagata, Y.: Nippon Steel & Sumitomo Metal Technical Report No. 105 December 2013. Available at: https://www.nipponsteel.com/en/tech/report/nssmc/pdf/105-06.pdf
[3] Technology. Seoul, Korea: Frontics Co., 2000 [cit. 2021-12-12]. Available at: http://www.frontics.com/en/d_report.php
[4] Pokorný, P., Dlhý, P., Poduška, J., Fajkoš, R., Vojtek, T., Náhlík, L., Grasso, M., Hutař, P.:. Theor. Appl. Fract. Mech., vol. 109, 2020, 102732.
[5] Guo, J., Fu, H., Pan, B., Kang, R.: Chinese Journal of Aeronautics, vol. 34, no. 2, 2021, p. 54-78.
[6] Totten, G.: Handbook of Residual Stress and Deformation of Steel. ASM International, Ohio, 2002.
[7] Tabor, D.: The Hardness of Metals. Oxford, London, 1951.
[8] Kim, Y.C., Song W.S., Kim J.H., Kim K.H., Kwon, D.: Procedia Eng., vol. 10, 2011, 10, p. 3162-3172.
[9] Kim, J.Y., Lee K.W., Lee J.S., Kwon, D.: Surf. Coat. Technol., vol. 201, no. 7, 2006, p. 4278-4283
[10] ISO/TR 29381. Metallic Materials - Measurement of mechanical properties by an instrumented indentation test - Indentation tensile properties. Switzerland: ISO, 2008
[11] FRONTICS, INC. Instrumented Indentation Technique (IIT). Seoul, Korea, April, 2012, 15 p.
[12] EN 13261:2009: E. Railway applications - Wheelsets and bogies - Axles - Product requirements. Cen, Brussel, 2009.

Powder Metallurgy Progress, Vol.22 (2022), No.1, p.025-030
http://dx.doi.org/10.2478/pmp-2020-0004

EFFECT OF THE PROCESSING ROUTES ON THE PROPERTIES OF CoCrFeMnNi ALLOY

Jaroslav Čech, Jiří Čapek, Filip Průša, Petr Haušild

Abstract
High entropy alloys are one of the most developing classes of materials of the 21st century. Their properties can significantly vary depending on their chemical composition and processing method. Thus, the microstructure and mechanical properties of CoCrFeMnNi high entropy alloy prepared by conventional casting, melt-spinning and mechanical alloying were investigated in this study. The observed structure and grain size were typical for this type of alloy and production methods. It was found that the hardness of the sample prepared by mechanical alloying with subsequent spark plasma sintering is higher compared to cast and melt-spun samples due to the finer microstructure and higher deformation energy stored.
Keywords: HEA, nanoindentation, microstructure, mechanical properties

INTRODUCTION

A lot of interest in the last two decades is paid to a new class of materials called high entropy alloys (HEAs). By definition, they are composed of at least five elements in equiatomic or nearly equiatomic concentration [1]. Although they consist of a high number of elements, the amount of phases is limited and often only one phase is present. The presence of only one phase and its stability gives to these alloys large application possibilities. Superior mechanical properties include high hardness, strength, and wear resistance even at elevated temperatures. Some of these alloys can be used also as diffusion barriers, magnetic, biocompatible, or radiation-resistant materials [1].

The amount of possible element combinations forming high entropy alloys is very large and it is not possible to describe all of them. For this reason, the model alloy is usually used as a characteristic representative for every class of HEAs. Many of HEAs with face-centered cubic (fcc) structure are derivatives of the so-called Cantor alloy composed of Co, Cr, Fe, Mn, and Ni in equiatomic ratios [2].

The microstructure and resulting mechanical properties of this alloy significantly depend on its processing route. Traditional melting and casting are one of the techniques used for the preparation of Cantor alloy. The properties of the arc melted alloy including thermomechanical processing are described for example in [3-6].

This work was presented at the conference Local Mechanical Properties 2022 held in Kosice, Slovakia on May 11-13, 2022.
Jaroslav Čech, Petr Haušild: Department of Materials, Faculty of Nuclear Sciences and Physical Engineering, Czech Technical University in Prague, Trojanova 13, 120 00 Praha, Czech Republic
Jiří Čapek: Department of Solid State Engineering, Faculty of Nuclear Sciences and Physical Engineering, Czech Technical University in Prague, Trojanova 13, 120 00 Praha, Czech Republic
Filip Průša: Department of Metals and Corrosion Engineering, Faculty of Chemical Technology, University of Chemistry and Technology Prague, Technická 5, 166 28 Praha, Czech Republic

Another technique used to produce CoCrFeMnNi alloy in the form of thin ribbons is melt-spinning (MS). As the melted alloy is put on the rotating wheel and quickly cooled, melt-spinning results in a fine-grained microstructure which is interesting for many applications [7-9]. In the last years, one of the favorite processing methods for grain refinement is spark plasma sintering (SPS) of mechanically alloyed (MA) powders [10-12]. Pure powders are homogenized by severe plastic deformation, repeated cold welding, and fracturing in a ball mill [13-14] and subsequently sintered by passing the electric current through the pressed powder. As in the case of melt-spinning, the process is fast and the resulting microstructure is very fine [15-17].

In the presented study, the mechanical properties of the Cantor CoCrFeMnNi alloy prepared by these three different techniques are investigated and correlated with the microstructural observations.

MATERIALS AND METHODS

Cantor alloy (i.e., CoCrFeMnNi in equiatomic portions) was prepared by three different techniques – induction melting, melt-spinning, and mechanical alloying with consequent spark plasma sintering. For the first sample, the ingot with a diameter of 14 mm and a length of 150 mm was prepared by induction melting in a protective Ar atmosphere at 1800 °C and homogenized for several minutes by eddy currents.

For melt-spinning, the alloy was melted in Ar atmosphere and ejected by Ar overpressure of 10×10^4 Pa to the surface of the water-cooled Cu wheel. The circumferential speed of the wheel was 30 m/s. The cooling of the resulting ribbons with an average thickness of 30 μm and width of 2-5 mm was finished by immersion in the water.

Mechanical alloying was carried out in a planetary ball mill (Retsch PM-100, Haan, Germany) with milling balls made of AISI 420 stainless steel. Powders of pure elements (Co (2 μm, 99.8%), Cr (44 μm, ≥ 99%), Fe (5-9 μm, 99.9%), Ni (10 μm, 99.5%), and Mn (≤ 10 μm, 99.6 %)) were blended to form the equiatomic mixture. 4 wt.% of n-heptane serving as process control agent was added for reducing the excessive cold welding. The ball-to-powder ratio was 15:1. The milling at a rotational speed of 400 rpm was executed under vacuum for 24 h. The homogenized powder was sintered in SPS machine HP D10 (FCT Systeme GmbH, Rauenstein, Germany) into a disc with a diameter of 20 mm. The heating and cooling rates were 100 °C/min. The maximum temperature was 1100 °C and pressure 48 MPa.

The microstructure of the samples was observed by scanning electron microscope Jeol JSM IT500HR (JEOL, Tokio, Japan), equipped with energy-dispersive spectrometer JED-2300, in the regime of back-scattered electrons on metallographic cuts. After standard preparation procedures (mechanical grinding and polishing using abrasive papers and diamond pastes, finishing by 0.04 μm colloidal silica), the microstructure was revealed by etching in HCl + HNO_3 + H_2O solution. PANalytical X'Pert Pro X-Ray diffractometer (PANalytical, Almelo, The Netherlands) in Bragg-Brentano geometry with Co cathode was used for the determination of phase composition of investigated samples.

Hardness and Young´s modulus were determined using NHT^2 nanoindentation tester (Anton Paar, Graz, Austria) with Berkovich diamond tip on polished cross-sections. As the thickness of the melt-spun samples was only about 30 μm, the maximum indentation load was limited to 100 mN to prevent the effect of surrounding material on the measured results. On the other hand, very small loads were avoided to reduce the influence indentation size effect. Therefore, based on the preliminary tests, the load was selected to reach the penetration depths of around 1 μm. Loading, holding at maximum load, and unloading were 30 s, 10 s, and 30 s, respectively. Data were analyzed by Oliver-Pharr

method [18] in accordance with ISO 14577 standard [19]. At least 10 indents were performed to obtain statistically significant values.

RESULTS AND DISCUSSION

The cast sample has large grains (Fig. 1(a)), which are typical for samples without any consequent thermo-mechanical treatment. More detailed observations (Fig. 1(b)) revealed substructural units (cells) of the size of several (tens of) micrometers.

A typical example of the microstructure of a melt-spun sample is shown in Fig. 1c. The thickness of the ribbon was about 30 μm. At the side, where the solidification started (bottom side of Fig. 3(c)), columnar grains were observed. With increasing distance from this side, grains were more equiaxed. Their average size in the direction of the ribbon axis was about 1-2 μm.

The SPS sample has the finest microstructure. Equiaxed grains had approximately 0.5 μm. Elemental mapping (Fig. 2) of the region near the center of the sample shows the presence of very small oxides and chromium carbides. The oxygen and carbon are impurities resulting from the production process (mechanical alloying with the subsequent SPS) and their content was significantly higher for the SPS sample than for the cast and melt-spun sample. Oxygen content in the SPS sample was about 5.2 at.% while only 0.7 at.% for the cast sample, and 1.9 at.% for the melt-spun sample. The amount of carbon was approximately two times higher for the SPS sample than for the other two samples. Although it is not possible to determine the content exactly by EDS technique due to the contamination, the content was in the order of units of at.%. No gradient of C content was observed from the surface to the center of the SPS sample, which means that the contamination originating from n-heptane used as a control agent is more significant than the effect of the graphite die used during the sintering process.

The microstructure of the samples corresponds well to the production technique. Large grains are typical for the cast samples, as the process is relatively slow. On the other hand, melt spinning and spark plasma sintering are very fast processes that do not enable coarsening of the microstructure.

X-ray diffraction patterns are presented in Fig. 3. As could be expected for CoCrFeMnNi alloy, a face-centered cubic phase was observed for all three samples. Moreover, small peaks of Fe_3O_4 oxides and second fcc phase or chromium carbide $Cr_{23}C_6$ were found in the SPS sample. The presence of oxides and carbides is in accordance with microstructural observations.

Results of the indentation measurements are presented in Tab. 1. The lowest hardness (2480 MPa) was observed for the cast sample. Only a slightly higher value (2971 MPa) was measured for the melt-spun sample. The hardest was the SPS sample (4162 MPa). These differences in hardness are the consequence of the processing route and corresponding microstructure. The coarse microstructure of the cast sample with large grains led to the lowest hardness. The reduction of the grain size of the melt-spun sample resulted in an increase in hardness. A more significant increase was observed for the SPS sample. It is caused not only because of the smaller grain size but mainly also by the presence of the second phase particles (i.e., oxides and carbides).

Young´s modulus of the cast (196 GPa) and SPS (219 GPa) sample was in good agreement with the literature data [20]. Only 176 GPa was measured for the melt-spun sample. This slightly lower value is probably the result of the surrounding material (phenolic resin). The volume of the material probed to obtain Young´s modulus is given by the elastic field around the indent which is significantly larger than the plastic field essential for hardness measurements [21]. Thus, even if the size of the indent fulfills the

restrictions (distance from the side of the sample) for the hardness measurements, it is not sufficient for precise evaluation of elastic properties, which are slightly underestimated in our case.

Tab. 1 Mechanical properties of CoCrFeMnNi samples.

	H (MPa)	**E (GPa)**
Casting	2480 ± 105	196 ± 11
Melt-spinning	2971 ± 218	176 ± 15
Spark plasma sintering	4162 ± 162	219 ± 7

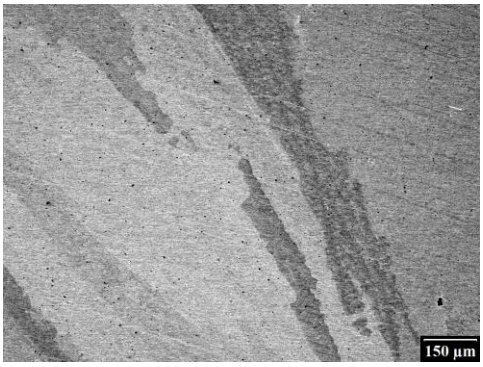

(a)

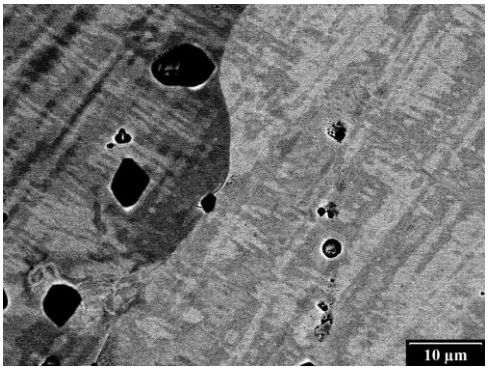

(b)

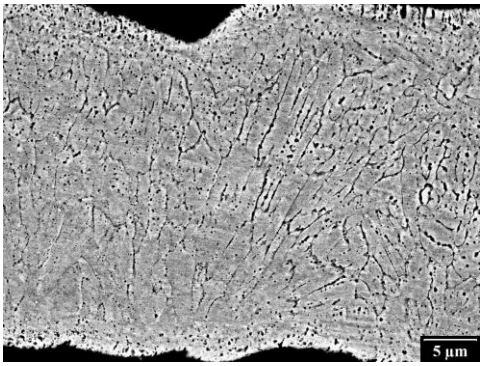

(c)

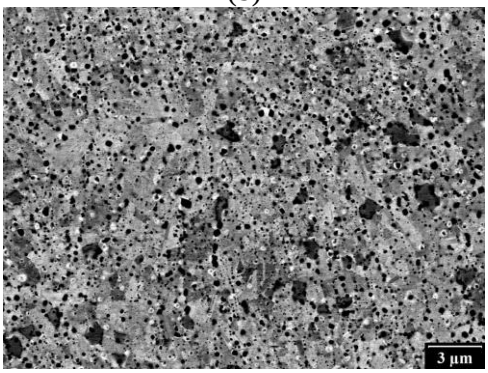

(d)

Fig. 1. Microstructure of CoCrFeMnNi samples a)-b) cast, c) melt-spun, d) SPS. SEM-BSE images.

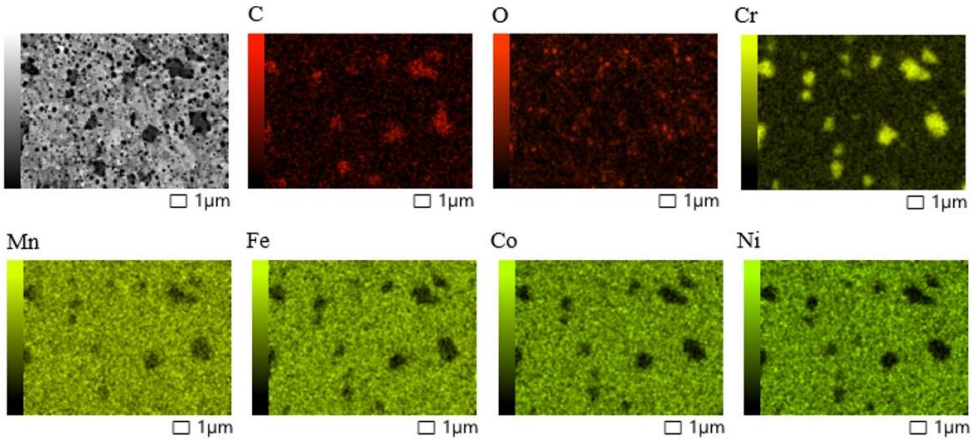

Fig. 2. Elemental map of CoCrFeMnNi spark plasma sintered sample.

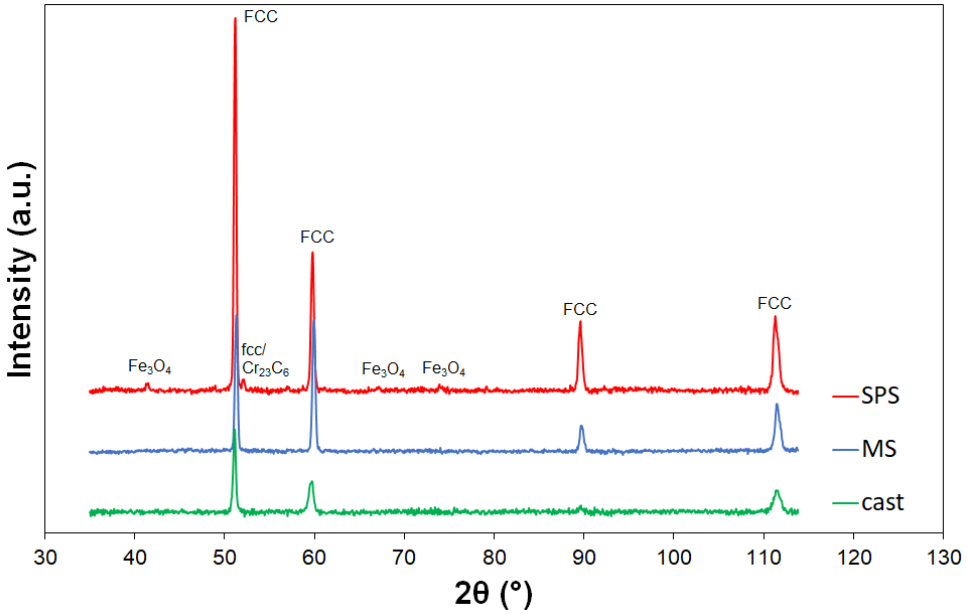

Fig. 3. X-ray diffraction of CoCrFeMnNi samples.

CONCLUSIONS

High entropy alloy CoCrFeMnNi was prepared by three different techniques (casting, melt-spinning, and spark plasma sintering). It was found that the processing route has a significant effect on the microstructure and consequently on the hardness of the material. The sample with the coarsest microstructure showed the lowest hardness and vice-versa. The high hardness of the SPS sample can be attributed to very low grain size and imposed plastic deformation. The results will be used as a basis for the development of materials with superior mechanical properties (strength, hardness, and toughness), which should be prepared by various combinations of high entropy alloys based on the CoCrFeMnNi system.

ACKNOWLEDGMENT

Financial support by the European Regional Development Fund in the frame of the project Centre of Advanced Applied Sciences (No. CZ.02.1.01/0.0/0.0/16_019/0000778), Czech Science Foundation (project No. 21-11313S) and Technology Agency of the Czech Republic (project No. TK01030108) is gratefully acknowledged.

REFERENCES

[1] Tsai, M.-H., Yeh, J.-W.: Mater. Res. Lett., vol. 2, no. 3, 2014, p. 107.
[2] Cantor, B., Chang, I.T.H., Knight, P., Vincent, A.J.B.: Mater. Sci. Eng. A, vol. 375-377, 2004, p. 213.
[3] Otto, F., Dlouhý, A., Somsen, Ch., Bei, H., Eggeler, G., George, E.P.: Acta Mater., vol. 61, 2013, p. 5743.
[4] Liu, W.H., Wu, Y., He, J.Y., Nieh, T.G., Lu, Z.P.: Scr. Mater., vol. 68, 2013, p. 526.
[5] Bhattacharjee, P.P., Sathiaraj, G.D., Zaid, M., Gatti, J.R., Lee, Ch., Tsai, Ch.-W., Yeh, J.-W.: J. Alloy. Compd., vol. 587, 2014, p. 544.
[6] Huang, Y.-Ch., Su, Ch.-H., Wu, S.-K., Lin, Ch.: Entropy, vol. 21, 2019, 297.
[7] Cantor, B., Kim, W.T., Bewlay, B.P., Gillen, A.G.: J. Mater. Sci., vol. 26, 1991, p. 1266.
[8] Xu, X.D., Liu, P., Guo, S., Hirata, A., Fujita, T., Nieh, T.G., Liu, C.T., Chen, M.W.: Acta Mater., vol. 84, 2015, p. 145.
[9] Chen, Ch., Zhang, H., Fan, Y., Zhang, W., Wei, R., Wang, T., Zhang, T., Li, F.: J. Magn. Magn. Mater., vol. 502, 2020, p. 166513.
[10] Průša, F., Šenková, A., Kučera, V., Čapek, J., Vojtěch, D.: Mater. Sci. Eng. A, vol. 734, 2018, p. 341.
[11] Vaidya, M., Anupam, A., Bharadwaj, J.V., Srivastava, Ch., Murty, B.S.: J. Alloy. Compd., vol. 791, 2019, p. 1114.
[12] Joo, S.-H., Kato, H., Jang, M.J., Moon, J., Kim, E.B., Hong, S.-J., Kim, H.S.: J. Alloy. Compd., vol. 698, 2017, p. 591.
[13] Suryanarayana, C.: Prog. Mater. Sci., vol. 46, no. 1-2, 2001, p. 1.
[14] Bhadeshia, H.K.D.H.: Mater. Sci. Technol., vol. 16, no. 11-12, 2000, p. 1404.
[15] Orru, R., Licheri, R., Locci, A.M., Cincotti, A., Cao, G.: Mater. Sci. Eng. R, vol. 63, no. 4-6, 2009, p. 127.
[16] Nová, K., Novák, P., Průša, F., Kopeček, J., Čech, J.: Metals, vol. 12, 2019, p. 20.
[17] Průša, F., Cabibbo, M., Šenková, A., Kučera, V., Veselka, Z., Školáková, A., Vojtěch, D., Cibulková, J., Čapek, J.: J. Alloy. Compd., vol. 835, 2020, p. 155308.
[18] Oliver, W.C., Pharr, G.M.: J. Mater. Res., vol. 19, no. 1, 2004, p. 3.
[19] ISO 14577, 2002.
[20] Haglund, A., Koehler, M., Catoor, D., George, E.P., Keppens, V.: Intermetallics, vol. 58, 2015, p. 62.
[21] Čech, J., Haušild, P., Karlík, M., Kadlecová, V., Čapek, J., Průša, F., Novák, P.: Mater. Tech., vol. 207, 2019, no. 2, p. 207.

Powder Metallurgy Progress, Vol.22 (2022), No.1, p.031-042
http://dx.doi.org/10.2478/pmp-2022-0005

MICROMECHANICAL PROPERTIES OF REACTIVE HiTUS TiNbVTaZrHf–N COATINGS ON DIFFERENT SUBSTRATES

František Lofaj, Tamás Csanádi, Lenka Kvetková, Petra Hviščová, Margita Kabátová, Alexandra Kovalčíková, Marek Vojtko, Vladimir Girman

Abstract

High entropy ceramic coatings, including multicomponent transition metal nitrides called also high entropy nitrides (HEN), are usually deposited using reactive arc and/or DC magnetron (co)sputtering. High Target Utilization Sputtering (HiTUS) was not applied in HEN systems up to now. Subsequently, the mechanical properties of HEN coatings prepared by HiTUS are also not known. The transition metals from the 4th and 5th group of the periodic table (Ti, Zr, Hf, Nb, V, and Ta) are strong nitride formers which would be the most suitable for HEN coating systems and therefore, investigation of their properties would be of significant interest. However, the nanoindentation measurements on thin coatings always produce „composite" values involving the contribution from the substrate. The separation of the coating properties from composite values requires upgraded analytical approaches different from standard Oliver & Pharr analysis. Thus, the aim work is to investigate the structure, hardness, and elastic modulus of TiZrHfNbVTa–xN coatings with different nitrogen stoichiometry deposited by reactive HiTUS using both CSM for bulk and CSM for thin films methods and to compare the results obtained on 4 different substrates (Si wafer, sapphire, 100Cr6 steel, and Ti6Al4V alloy). The subsequent results showed systematic differences in the calculated mechanical properties depending on the substrate properties both in CSM and CSMTF modes. Stiffer substrates always resulted in the overestimations of the calculated hardness and indentation modulus compared to softer substrates with lower Young's modulus and the differences were in the range of around 10 %. Obviously, better theoretical models for the calculations of true coating properties are required.

Keywords: high entropy nitride, HiTUS, thin coatings, nanoindentation, substrate influence, mechanical properties of thin coatings.

INTRODUCTION

High entropy ceramics (HEC) coatings, including multi-component transition metals (TM) forming high entropy nitride (HEN) coatings, are usually deposited using reactive arc and/or DC magnetron (co)sputtering [1]. The recent sputtering method called High Target Utilization Sputtering (HiTUS) was not applied in HEN systems up to now.

This work was presented at the conference Local Mechanical Properties 2022 held in Kosice, Slovakia on May 11-13, 2022.

Lofaj František, Csanádi Tamás, Kvetková Lenka, Hviščová Petra, Kabátová Margita, Kovalčíková Alexandra, Vojtko Marek, Girman Vladimir: Institute of Materials Research of the Slovak Academy of Sciences, Watsonova 47, 04001 Košice, Slovakia

Thus, despite strong indications from W-C:H coatings [2] it was not confirmed yet that HiTUS is suitable for the generation of high entropy solid solutions from multicomponent transition metals and their solid solution nitrides. Subsequently, the mechanical properties of HEN coatings prepared by HiTUS are also not known. The transition metals from the 4th and 5th group of the periodic table (Ti, Zr, Hf, Nb, V, and Ta) are strong nitride formers found to be suitable for HEN with improved thermal and mechanical properties [3]. Thus, 6-component high entropy solid solutions of all strong nitride formers are of significant interest. The optimization of their preparation by new HiTUS technology requires precise measurements of their mechanical properties which are usually done by nanoindentation.

The nanoindentation testing on thin hard coatings always generates „composite" values because of the simultaneous involvement of the contribution from more compliant substrates. The extraction of the coating properties from composite values requires approaches different from standard Oliver & Pharr (O&P) analysis applied to bulk materials and single loading-unloading tests [4]. Instead of single hardness and modulus values calculated from one penetration depth, corresponding depth profiles obtained from a series of single tests covering the range of depths from tens of microns up to a depth comparable with the thickness of the coating are required. Analogous hardness and indentation modulus depth profiles can be obtained from repeated re-loadings after partial unloadings during an interrupted single-loading test. This testing mode is called „cyclical indentation testing" or „continuous multicycle" (CMC). Another mode is based on small additional sinusoidal unloadings during standard continuous loading. This mode, applied to bulk materials, is called „sinusoidal loading" or „continuous stiffness measurements" (CSM) [5-9]. Since the average values obtained from the series of standard single loading-unloading tests and those of the sinusoidal tests were the same [8], CSM became the most attractive among all modes. Besides offering full stiffness, hardness, and modulus depth profiles from each indentation test, it requires considerably shorter measurement time and the effects of thermal drift and low-frequency noise on the measurements are dramatically reduced [8-9] compared to standard modes. On the other hand, the largest disadvantage of CSM during continuously increasing load compared to quasi-static tests is the contribution of „plasticity error" [10], which can result in sufficient deviations from true values, especially in the materials with high E/H ratio and at lower frequencies [8, 10]. Plastic error is a consequence of additional plastic deformation on top of elastic deformation during the loading part of each cycle resulting from the small increase in the load compared to that in the previous cycle. Fortunately, it can be reduced via correction and/or selection of appropriate amplitude and frequency of CSM testing [10]. Analytical corrections and even experimental procedure resulting in a significant reduction of plasticity error, as well as other factors (e.g. phase lock amplifier time constant, unloading curvature, and load frame stiffness), was proposed in [9]. Another possibility to eliminate plasticity error is to use the recently introduced Quasi-CSM (QCSM) mode when sinusoidal oscillations are applied only to repeated, short dwell-time periods during a continuous loading cycle [11].

The above-mentioned studies were concerned only with the improvement of the accuracy of the data measured by CSM mode used for the depth profile determination, not by the extraction of the properties of the coating from the measured profile. The practical approach to do it is based on the procedure recommended by the ISO 14577-4:2016 standard, developed for thin films. The true modulus of hard coating on a softer substrate can be determined by the extrapolation of the values from the plateau at the maximum of the corresponding profile to zero penetration depth (load) [12]. The lower boundary of the plateau range used for the extrapolation should be greater than the diameter of the indenter tip and the upper boundary at relative depths within 10 % of the coating thickness [4]

The analytical models developed for extracting coating modulus from the modulus-depth profile are based on the assumption of various interactions between coating and substrate. The first model by Doerner and Nix assumed linear interaction with the experimentally determined coefficient [13]. The more sophisticated model of Gao [14] was further refined by Menčík [15] and Song-Pharr [16]. The models of Bull [17] and Puchy-Cabrera [18] assumed different functions describing coating/substrate interactions. However, the applicability of these models is limited because none of these was able to predict the response with sufficient accuracy in case that the elastic modulus of the coating was more than two times higher than the modulus of the substrate [19]. The reason is that in the Gao-based models, the material under the indenter is considered to be isolated from the surroundings. However, it is not the case, especially for very stiff coatings which can provide additional support against the deformation of the substrate. That is why Hay and Crawford [19] proposed further refinement of Song-Pharr's model [16] which accounts for the additional influence of the coating on the substrate. The method of calculation based on this model is commercially available as „CSM for thin films" (CSMTF). The parameters for the calculation of the corresponding depth profiles involve Young's modulus and Poisson's ratio of the substrate and thickness of the coatings. Principal advantage of the Hay and Crawford model is that it is applicable up to a 10-fold ratio between the elastic moduli of coating and substrate. Moreover, the range of relative indentation depths which can be used for the determination of corresponding mechanical properties expands up to 40 % which is considerably more than common 10 % relative depth. On the other hand, direct comparison of the values of hardness and indentation modulus obtained by the standard CSM procedure and the values measured by CSMTF on the same coatings are still missing.

The aim of the current work is to compare the results obtained from CSM and CSMTF on coatings deposited on the substrates with very different elastic moduli. The HEN TiZrHfNbVTa–N_x coatings with different nitrogen stoichiometry deposited by reactive HiTUS on 4 different substrates ((111) Si wafer, (0001) sapphire, polycrystalline 100Cr6 steel, and Ti6Al4V alloy) were investigated using both CSM for bulk and CSM for thin films modes.

MATERIALS AND METHODS

A set of TiNbVTaZrHf-N (the abbreviation 6TM-N will be used for simplification) coatings was deposited using reactive High Target Utilization Sputtering (model S500, Plasma Quest Ltd., UK) from 76.2 mm (3 inches) Ti-Nb-V-Ta-Zr-Hf target (Ti – 20 at. %, Nb – 18 at. %, V – 20 at. %, Ta –18 at. %, Zr –12 at. %, Hf –12 at.%, Kurt Lesker, GB) on polished (0001) sapphire and (111) Si wafer substrates simultaneously. In some cases, additional polished 100Cr6 steel and Ti6Al4V substrates were also used. The roughness values of the substrates after polishing were typically below 20 nm. The reactive sputtering was carried out by additions of variable amounts (flow) of nitrogen into Ar sputtering atmosphere. For improved adhesion, a metallic interlayer from the same target, with a thickness of up to 200 nm, was used before the introduction of the nitrogen into the chamber.

The optimum deposition parameters of the HiTUS were determined in our previous research [2, 20-22] and involved constant RF power on PLS (plasma source) of 1800 W, RF target power of 700W, 5 W of RF bias, deposition temperature of 300 ^{O}C, and deposition time of 90 min. The flow rates of the reactive gas (nitrogen) were in the range from 0 to 10 standard cubic centimeters per minute (sccm). That caused an increase in the working pressure from $7.5x10^{-6}$ mbar to up to $8.1x10^{-3}$ mbar. The obtained thicknesses of

the coatings were reduced from around 1780 nm without nitrogen to 1200 nm at 10 sccm nitrogen.

Based on the recommendations made in [10] the nanoindentation measurements were performed in CSM mode and the CSM for thin films CSMTF mode [19] with Berkovich diamond tip at the constant strain rate of 0.05 s^{-1}, an amplitude of 2 nm and frequency of 45 Hz. in a standard nanoindenter (model G200, Agilent, USA). Two independent sets of 16 indents up to 600 nm depth were carried out on each coating. The indenter tip area was calibrated on fused silica after each ~300 indents. The minimum depth resulting from tip area calibration was usually around 80 nm. In CSM cases, the extrapolation was performed from the plateau or maximum on the hardness and modulus profiles with the maximum depth below 10 % of the coating thickness. The calculation of the indentation modulus in CSMTF required input of coating thickness as well as Poisson's ratio and Young's modulus of the substrate. Tabulated values of these parameters were used for the selected substrates (see Tab. 1). The thickness of the coatings was measured using scanning electron microscopy (SEM, models Auriga Compact and EVO MA15, Zeiss, Germany) on the fractured cross sections of the coatings deposited on Si wafers. The upper limit of the relative depth range used for extrapolation may exceed 10 % but the width of that range was always at least 3–5 % of the indent depth.

Tab. 1 Mechanical properties of the substrates ($^{\#}$ - measured on polished substrates by nanoindentation in CSM mode).

Substrate type	Young's modulus E, GPa	Poisson's ratio ν, -	$H_{IT}^{\#}$ GPa	$E_{IT}^{\#}$ GPa
(111) Si wafer	187	0.223	13.07±0.13	193.6±1.2
(0001) sapphire wafer	435	0.29	27.57±0.27	458.7±3.3
tempered 100Cr6 steel	210	0.285	9.25±1.0	250.0±9.5
Ti6Al4V alloy	115	0.34	5.20±0.16	133.2±2.2

EXPERIMENTAL RESULTS AND DISCUSSION

Coating preparation

The current study was performed on a set of seven TiZrHfNbVTa–xN coatings prepared with different amounts of nitrogen in the sputtering Ar atmosphere thus resulting in different stoichiometry. Six coatings were deposited on thin (111) Si and (0001) sapphire wafer substrates. The deposition conditions and the coating thicknesses are summarized in Tab. 2 The TiZrHfNbVTa–6N coating obtained at 6 sccm N_2 flow, was selected for a more detailed investigation. For that reason, additional coating was deposited at 6 sccm flow on Si and sapphire as well as on the polished discs of 100Cr6 steel and Ti6Al4V alloy to cover wide range of elastic moduli ratios of coating vs. substrate (see in Tab. 1).

Tab. 2 The list and the conditions for the deposition of the studied multicomponent high entropy nitride TiZrHfNbVTa–xN coatings prepared by reactive HiTUS. The constant deposition parameters include PLS RF power – 1800 W, RF target power – 700 W, bias – RF 5W, and deposition time – 90 min. The target to-substrate distance was 17 cm. (* – deposited on 4 different substrates).

Sample	N_2 flow, sccm	Working pressure, Pa	Coating thickness, nm
6TM – 0N	0	0.78	1705
6TM – 2N	2	0.8	1780
6TM – 4N	4	0.8	1610
6TM – 6N	6	0.8	1620
6TM – 6N*	6	0.8	1324
6TM – 8N	8	0.81	1420
6TM – 10N	10	0.81	1210

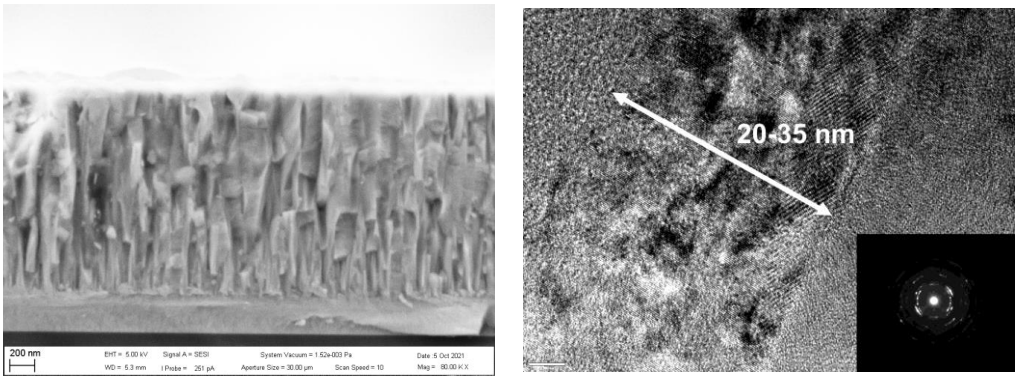

a) b)

Fig. 1. Structure of the studied 6TM-6N coating on (100) Si substrate: a) SEM micrograph of the fracture surface suggesting a textured columnar structure. The thickness of the coating is around 1600 nm; b) a high-resolution TEM and selective area electron diffraction (SAED) confirming textured nanocrystalline structure.

The amount of nitrogen added to the Ar sputtering atmosphere influenced not only the deposition rates (thicknesses of the coatings) and concentrations of nitrogen (stoichiometry) but also their structures [23]. Metallic coatings (without nitrogen addition) exhibited featureless fracture surfaces, which is typical of an amorphous structure. The fracture surface of the coatings deposited with more than 4 sccm N_2, exhibited intercrystalline fracture suggesting the presence of columnar structures. High-resolution TEM confirmed the presence of composite structure with (nano)crystalline columns in the amorphous matrix (Fig. 1(b)). The diameters of the columnar grains were 30 nm and they were mostly oriented in <111> direction.

CSM vs. CSMTF

The work involves the comparison of the results obtained by two different techniques – CSM for bulk materials and CSMTF applicable for thin films. The tests were

performed independently in two 16-indent matrices located 200 μm apart to avoid the possible effects of the coating's variations. Fig. 2(a–d) shows the topography of the coatings and the indents obtained on Si wafer and sapphire substrates, respectively. The morphology of the coatings exhibited fine and homogeneous roughness regardless of the substrate. Roughness influence was not considered because it is mostly related to the scatter and not to the absolute values of the corresponding properties. The indents were very similar, no differences among them can be distinguished, neither in dependence on the technique nor on the substrate type. The only difference may be related to the appearance of small "frame" cracks on the Si wafer oriented along the indent edges. However, the relative penetration depth was intentionally set to below 30 % of coating thickness (600–800 nm) which means that the deformation of the substrate controlling cracking around the indents, would be only in a very early stage. Obviously, higher plastic deformation of Si substrate with lower Young's modulus and hardness can be expected after indentation at the same load than on stiffer and harder sapphire. Cracking in the coating would be therefore more probable on Si, which explains the absence of cracks in the sapphire case. On the other hand, it emphasizes different nanoindentation conditions in the coating resulting from different substrates.

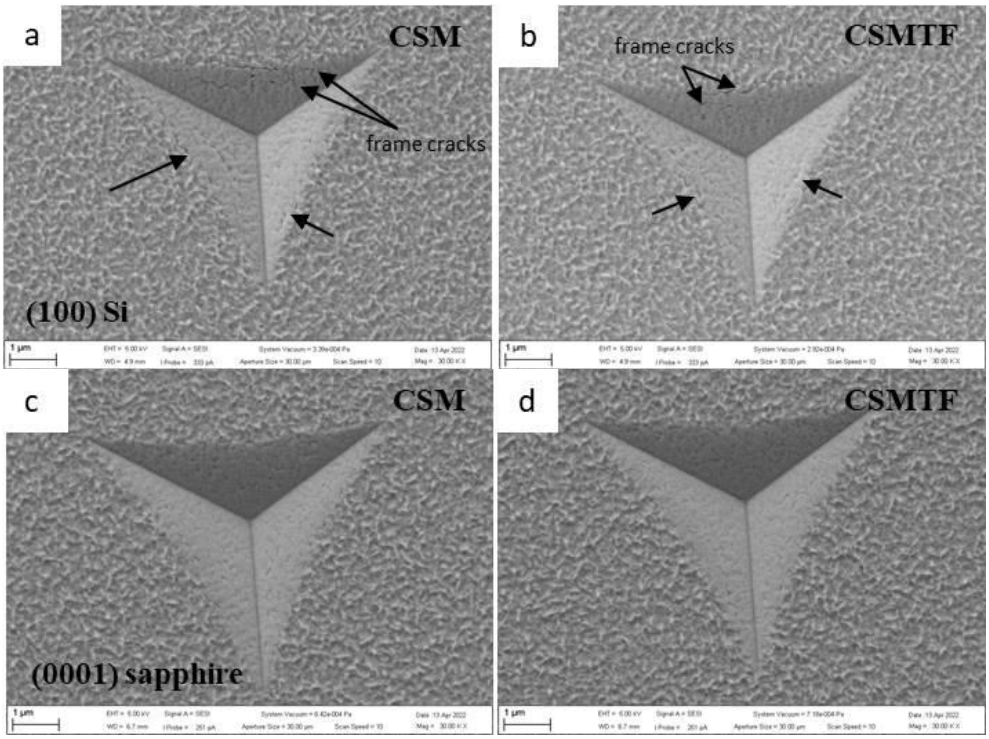

Fig. 2. Topography of the indents obtained at 600–800 nm penetration depth on reactive HiTUS TiZrHfNbVTa–6N coating deposited on (100) Si wafer using a) CSM and b) CSMTF modes; on (0001) sapphire wafer using c) CSM and d) CSMTF modes

However, cracking is out of the scope of this work which is focused on the extraction of coating properties in the depths within a couple of hundredths of nanometers.

The plots in Fig. 3 compare depth profiles of the average hardness and indentation modulus obtained on the same coating/substrate samples using CSM and CSMTF techniques. Both profiles exhibit a rapid increase during the first 50 nm of indentation depths attributed to the indenter tip geometry. The maxima were achieved below 100 nm depths which is in agreement with the lower limit of surface tip area calibration.

In the case of hardness profiles (Fig. 3(a)), relatively wide plateau with constant values occurs up to 150 nm in CSM and up to 250 nm depth in CSMTF cases. At larger depths, the composite hardness values gradually decreased. The situation in the case of indentation moduli profiles (Fig. 3(b)) was slightly different. The maxima were obtained at different depths, they did not overlap, small plateau was present only in CSMTF case and it spread only up to approximately 120 nm. The extrapolation to zero depth from the plateau within the 80–120 nm depth range was, therefore, more reliable in CSMTF than in CSM case, despite the resulting indentation moduli were almost identical. The differences between hardness – and indentation-modulus-depth profiles are a natural consequence of the higher sensitivity of the elastic stress field to the substrate due to the absence of elastic limit analogous to yield stress for plastic deformation. Thus, elastic deformation of the substrate is always present and reduces the width of the plateau compared to that of the hardness. Another advantage of CSMTF is that the contribution of the substrate is reduced to a larger extent than in CSM. That is readily visible in the difference between composite values obtained by these techniques at depths exceeding 300 nm. Thus, the main advantages of CSMTF technique, compared to CSM, are the better elimination of the contribution of the substrate and wider plateau at maxima which increases the reliability of the determined coating properties, obtained by the extrapolation procedure to zero depth. On the other hand, the values obtained by CSMTF are dependent on coating thickness, elastic modulus, and Poisson's ratio of the substrate.

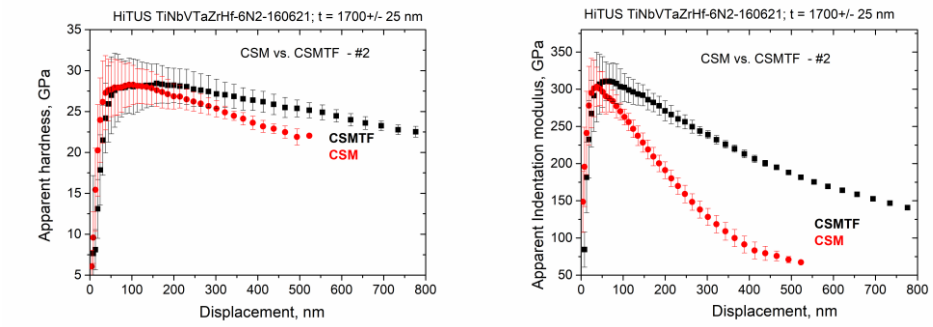

Fig. 3. The comparison of a) hardness and b) indentation modulus; depth profiles obtained on Si wafer in reactive HiTUS TiZrHfNbVTa–6N coating using CSM and CSMTF modes.

Effects of coating thickness and substrate properties in CSMTF

The model [19] assumes complex interaction between coating and substrate during nanoindentation. The elastic modulus of the coating, E_c, is calculated from the shear modulus, μ_c, and Poisson's ratio, ν_c, of the coating as [19]

$$E_c = 2\mu_c(1+\nu_c) \quad (1)$$

where

$$1/\mu_c = (1-I_0)/(\mu_c + F.I_0.\mu_c) + I_0/\mu_c, \quad (2)$$

F is a constant, which has to be determined experimentally, and I_0 is a complex weighing function introduced by Gao [14]. This function primarily depends on the parameter t/a = x, equal to the ratio of coating thickness t, and radial size of the indent, as:

$$I_0 = (2/\pi) \arctan(x) + (2\pi (1-\nu_a))^{-1}\{(1-2\nu_a) x \ln [(1 + x^2)/x^2] - x/(1 + x^2)\} \quad (3)$$

The parameter ν_a is an apparent Poisson's ratio depending on the Poisson's ratios of the coating, the substrate, and I_1 which is another function of the relative thickness x (see [19] for details). Because of the rather complex dependence of the elastic modulus of the coating resulting from Eq. 1-3, the influence of the variations of thickness and Young's modulus of the substrate were determined numerically. Figs. 4(a) and 4(b) illustrate the changes in the calculated indentation modulus and hardness with the variations of the true thickness and true Young's modulus of the substrate. The experimental data were obtained from the measurements on a second coating deposited with 6 sccm N_2 on a sapphire substrate with a thickness of 1324 nm. The plot in Fig. 4(a) shows that an underestimation of the coating thickness of up to 500 nm caused a little (<1%) decrease in the indentation modulus and an increase in hardness and vice versa. Evidently, the calculation of these values is not very sensitive to the thickness variations up to a third of the coating thickness and 100–200 nm deviation in thickness would cause negligible changes in the calculated values. On the contrary, the deviations in the modulus of the substrate had different influence on the calculated properties of the coating. The hardness values were not affected by substrate modulus deviations at all whereas elastic modulus changed almost exponentially. The underestimation of the substrate modulus of the sapphire by 50 GPa led to an overestimation of the calculated modulus of the coating by 11.5 % relative to the true value of the modulus. Analogous 50 GPa overestimation caused a smaller (~6 %) decrease due to the inverse exponential character of the dependence. Thus, Fig. 4(b) clearly shows that the indentation moduli evaluated by the CSMTF model are strongly dependent on the elasticmodulus of the substrate. The influence of the Poisson's ratio of the substrate has a minor influence on the calculation and it was not considered.

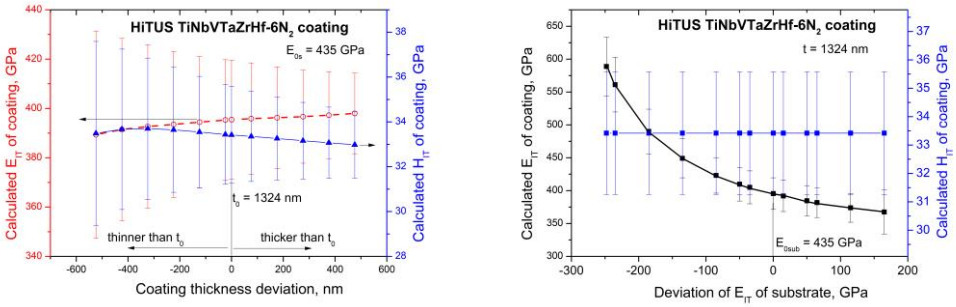

a) b)

Fig. 4. The influence a) of the error in the measurement of coating thickness and b) of the error in an indentation modulus of the substrate on the calculation of indentation modulus and hardness of TiZrHfNbVTa–6N coating based on Hay-Crawford model [19].

Substrate effects

The mechanical properties of TiZrHfNbVTa–6N coating, deposited on four different substrates and calculated with the thickness of 1324 nm measured by SEM and substrate elastic moduli, indicated in Tab. 2, are plotted in Fig. 5 vs. the elastic modulus of the substrate. The range of substrate elastic moduli spanned from ~120 GPa up to 435 GPa which is almost a 300 % difference. The ratios between the moduli of the coating and substrate were in the range from <1.0 on sapphire up to <2.7; on Ti alloy which means that our study covers a relatively narrow range of ratios.

The influence of TiZrHfNbVTa interlayer on the calculated properties was neglected in our considerations because its hardness and indentation modulus (see Fig. 6 at 0 sccm N_2) are very similar to those of Si wafer and Ti-alloy substrates. Moreover, interlayer thickness of 200 nm is only 12–15 % of coating thickness. Thus, relatively small influence can be expected even on harder and stiffer sapphire substrate.

Despite the significant scatter at each measurement and even between two independent measurements, the data in Fig. 5(a) shows a systematic difference between CSM and CSMTF, and a dependence of the elastic moduli on the substrate modulus, especially at lower values of the substrate moduli. Up to the steel substrate, the calculated (average) values from CSMTF tests were ~15–19 % higher than those from the CSM tests. On the sapphire substrate, the difference was reverted and it was around 8 % smaller (but within the scatter of the measurements). At the same time, a tendency for a substantial increase of the calculated values from around ~260 GPa up to ~370–400 GPa with the increase of substrate stiffness was observed. The relative difference in the calculated values of E_{IT} was in the range of 35 % to 55 %, which is well above the acceptable limit of 5 %. Evidently, the influence of the substrate in the CSMTF model was not fully eliminated.

Variations in the calculated hardness were also present but the differences between the values calculated within CSM and CSMTF models were usually within the error limit. The maximum difference between average values was within 2 % which is acceptable. Such behavior is reasonable because no dependence on substrate modulus was built-in into Eq. 1–3 (see Fig. 4(b)) and all the data in Fig. 5(b) seem to reflect the statistical scatter among analogous measurements, rather than the difference between CSM and CSMTF. Thus, the calculations of hardness based on standard CSM and CSMTF provide sufficiently reliable data with comparable accuracy.

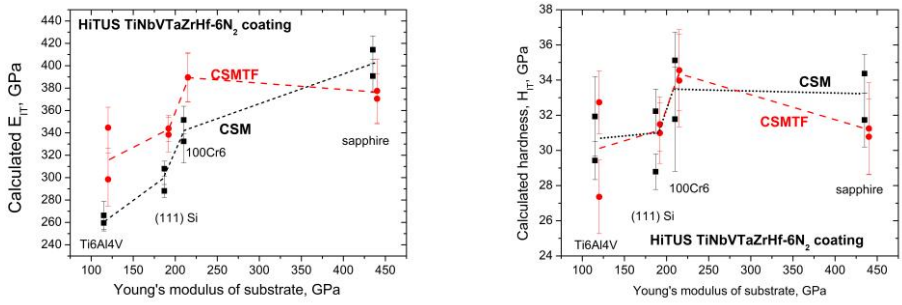

a) b)

Fig. 5. The comparison of the calculated values of a) indentation modulus, and b) hardness, in dependence on Young's modulus of the substrate obtained using CSM and CSMTF

models. The data from CSMTF were intentionally offset for better visibility of the error bars.

The above results indicate that CSM and CSMTF models involve systematic and a sufficiently large influence on the absolute values of indentation modulus while the influence on the calculated hardness is much smaller. To reduce the strong effect of the properties of the substrate (on E_{IT}) on the determination of elastic properties of the coatings within the existing CSMTF model, it is reasonable to use the same substrate for the measurements and calculations on the whole series of coatings.

Hardness and elastic modulus of TiZrHfNbVTa–xN coatings

Fig. 6 summarizes nanoindentation results of the all series of TiZrHfNbVTa – xN coatings deposited on silicon and sapphire wafers by reactive HiTUS vs. the amounts of nitrogen (see Tab. 2) added into the sputtering Ar atmosphere. The average values of calculated hardness and indentation moduli were systematically shifted: the values on the Si wafer were practically always lower than those on the sapphire by <10% and 8%, respectively. However, the same dependencies were produced by both substrates. The mechanical properties of the metallic coating without nitrogen exhibited the lowest values and even a small amount of nitrogen caused their substantial increase. The maximum and/or saturation were achieved already at about 4 sccm of nitrogen. Further increase of nitrogen flows above 6 sccm caused small degradation of the corresponding properties. Thus, despite the almost 10 % systematic difference in the absolute values of hardness and indentation modulus of the coatings, these dependencies can be successfully used for the optimization of the reactive HiTUS processes.

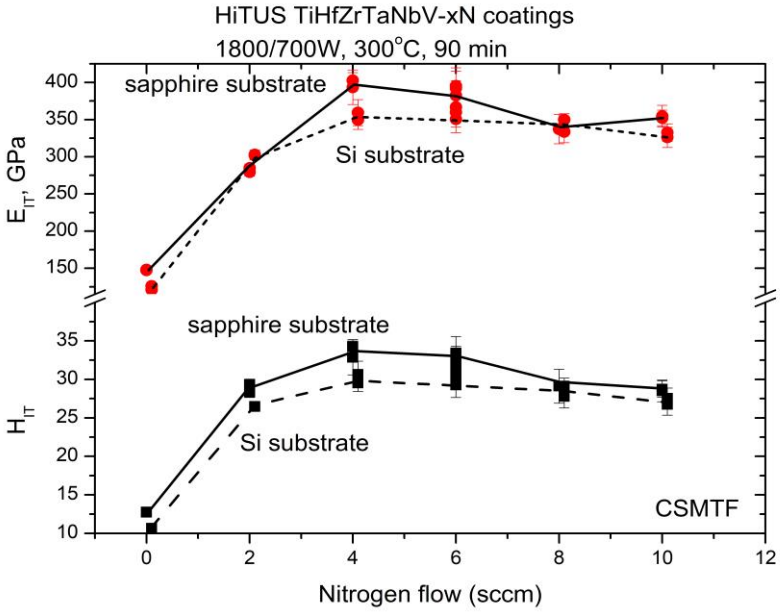

Fig. 6. A comparison of the values of hardness and indentation modulus of TiZrHfNbVTa–xN coatings deposited simultaneously on Si and sapphire wafers calculated using CSMTF model.

Fig. 6 confirms the observations from Fig. 5 implying that the calculation on more compliant Si substrates generate around 10 % lower elastic moduli and only slightly lower hardness values than in the case of stiffer sapphire substrates. Despite the exact differences between the effects of substrates depend on the number of measurements and corresponding statistics, systematic differences among the calculated elastic moduli in Fig 6 suggest that the role of substrate modulus in Eq. 2 is underestimated.

The maximum absolute hardness values of TiZrHfNbVTa–xN coating involving the differences resulting from the substrate effect were in the range from 28 GPa up to 34 GPa, the indentation moduli from 350 GPa to 390 GPa. These hardness values overlap with the 32.5–35 GPa while the indentation moduli were lower than 460–490 GPa reported for analogous nitride coatings deposited by DC magnetron sputtering in [3]. Despite differences in elastic moduli, it is confirmed that reactive HiTUS is suitable for the deposition of hard multicomponent nitride coatings similarly as in the case of carbide coatings [2, 20-22] and the obtained properties are comparable to those in DC and HiPIMS made coatings.

CONCLUSIONS

The nanoindentation tests on reactive HiTUS-made multicomponent transition metal-nitride coatings with different stoichiometry, deposited on the substrates with different Young's moduli and employing different measurement modes, revealed that:

- reactive HiTUS is a technique suitable to deposit multicomponent (high entropy) nitride coatings with mechanical properties comparable to those produced by most of the conventional sputtering techniques (DC magnetron sputtering and HiPIMS);
- both CSM and CSMTF methods of nanoindentation data treatment provide comparable values of hardness but CSM tends to underestimate elastic modulus on more compliant substrates;
- the modulus of elasticity calculated within the CSMTF model is highly sensitive to the underestimation of Young's modulus of the substrate;
- the effects of substrate compliance (and coating thickness) in the CSMTF model are not fully eliminated and further refinement of the coating/substrate interaction is required.

ACKNOWLEDGMENT

This work was supported by the Slovak Academy of Sciences via International Visegrad Fund (project JP39421 of V4-Japan Joint Research Program) and Slovak Research and Development Agency (projects APVV 17-0059, APVV-17-0320 and APVV-17-0049). The equipment used in the work was acquired from the project "Advancement and support of R&D for "Centre for diagnostics and quality testing of materials" in the domains of the RIS3 SK specialization, ITMS2014: 313011W442.

REFERENCES

[1] Lewin, E.: J. Appl. Phys., vol. 127, 2020, p. 160901.
[2] Lofaj, F., Hviščová, P., Zubko, P., et al.: Int. J. Refrac. Met. Hard Mat., vol. 80, 2019, p. 305-314.
[3] Kirnbauer, A., Kretschmer, A., Koller, C.M., Wojcik, T., Paneta, V., Hans, M., Schneider, J.M., Polcik, P., Mayrhofer, P.H.: Surf. Coat. Technol., vol. 389, 2020, p. 125674.
[4] Oliver, W.C., Pharr, G.M.: J. Mater. Res., vol. 7, 1992, p. 1564
[5] Oliver, W.C., Pethica, J.B.: Method for continuous determination of the elastic stiffness

of contact between two bodies, U.S. Patent 4 848 141, 18 July 1989, 1989.
[6] Li, X., Bhushan, B.: Mater. Char. vol. 48, 2002, p. 11
[7] Hay, J., Agee, P., Herbert, E.: Exp. Tech., vol. 34, 2010, p. 86
[8] Sudharshan Phani, P., Oliver, W.C., Pharr, G.M.: J. Mater. Res. vol. 36, 2021, p. 1740
[9] Sudharshan Phani, P., Oliver, W.C., Pharr, G.M., J. Mater. Res., vol. 36, 2021, p. 2137
[10] Merle, B., Meier-Kiener, V., Pharr, G.M.: Acta Mater., vol. 134, 2017, p. 167.
[11] Lorenz, L., Chudoba, T., Makowski, S., Zawischa, M., Schaller, F., Weihnacht, V.: J. Mater. Sci., vol. 56, 2021, p. 18740
[12] ISO 14577-4:2016 Metallic materials: instrumented indentation test for hardness and material parameters – part 4: test method for metallic and non-metallic coatings, (2016).
[13] Doerner, M.F., Nix, W.D.: J. Mater. Res., vol. 1, 1986, p. 601.
[14] Gao, H., Chiu, C-H., Lee, J.: Int. J. Solid Struct., vol. 29, 1992, 2471.
[15] Menčík, J., Munz, D., Quandt, E., Weppelmann, E.R., Swain, M.V.: J. Mater. Res. 12, 1997, p. 2475.
[16] Rar, A., Song, H., Pharr, G.M.: in Thin Films: Stresses and Mechanical Properties IX, eds. Ozkan, C.S., Freund, L.B., Cammarata, R.C., Gao, H.: Mater Res. Soc. Symp. Proc. vol. 695, Warrendale, PA, 2002. p. 432 [17] Bull S.J: Phil. Mag., vol. 95, 2014, p. 1907.
[17] Puchy, V., Cabrera, E.S., Staia, M.H., Iost, A.: Thin Solid Films, vol. 583, 2015, p. 177.
[18] Hay, J., Crawford, B.: J. Mater. Res., vol. 26, 2011, p. 727 .
[19] Lofaj, F. Kvetková, L., Hviščová, P., Gregor, M., Ferdinandy, M.: J. Eur. Ceram. Soc., vol. 36, 2016, p. 3029.
[20] Lofaj, F., Kabátová, M., Kvetková, L., Dobrovodský, J.: J. Eur. Ceram. Soc., vol. 40, 2020, p. 2721.
[21] Lofaj, F., Kabátová, M., Kvetková, L., Girman, V.: Surf. Coat. Technol., vol. 375, 2019, p. 839.
[22] Lofaj, F., Kvetková, L., Roch, T., Dobrovodský, J., Girman, V., Kabátová, M., Beňo, M.: Reactive HiTUS TiNbVTaZrHf-Nx coatings: structure, composition and mechanical properties, in preparation for Materials, 2023, vol.16(2), p. 563.

Powder Metallurgy Progress, Vol.22 (2022), No.1, p.043-052
http://dx.doi.org/10.2478/pmp-2022-0006

INVESTIGATION OF HYBRID LAP WELDS OF TI6AL4V AND STAINLESS STEEL WITH BRONZE INTERLAYER

Hana Chmelíčková, Martina Havelková, Aneta Hrubantová, Vlastimil Jílek, Lukáš Václavek, Tomáš Ingr

Abstract

Welding of the austenitic stainless steel AISI 304 and Ti6Al4V is complicated by hard and brittle intermetallic compound formation. In this contribution, we study a laser welding method that partially overcomes this problem using interlayer. Bronze foil (CuSn6) of thickness 100 µm and 200 µm was inserted between steel and titanium sheets and lap welds were realized on pulsed Nd:YAG laser. Representative samples were investigated by nanohardness measurement, SEM/EDS, and XRD analysis to detect the localization of the intermetallic phases. The macrostructure of the weld cross sections was displayed by optical and digital microscopy. The nano-hardness test revealed the presence of very hard intermetallic mainly around the interface between the fusion zone and bottom metal sheet. EDS mapping displayed the main elements Fe, Cr, Cu and Ti distribution in the fusion zone, EDS line scanning detected elements` signals in the diagonal and horizontal directions. XRD analysis revealed expected intermetallic compounds FeTi and $CuTi_2$ and solid solution $Cu_{0.8}Fe_{0.2}$.

Keywords: Ti6Al4V alloy, AISI 304 stainless steel, CuSn6 interlayer, Nd:YAG welding

INTRODUCTION

The joining of the austenitic stainless steels AISI 304, 304L, or 316L and the titanium alloy Ti6Al4V is subject of the world research with the aim to overcome a problem with the large difference in physical properties of these construction materials, that causes the formation of inter-metallic compounds (IMC) not only from the main elements iron and titanium (Fe_2Ti, FeTi) but also from steel alloying elements chromium and nickel ($TiCr_2$, $NiTi_2$, Ti/Fe/Cr) [1]. High residual stresses in the inhomogeneous fusion zone cause cracks propagation through these hard and brittle IMCs. Methods of the defect-free joining of the stainless steel and Ti6Al4V were developed in several ways. Direct joining is possible with diffusion or friction welding methods far below melting temperatures [2]. Fusion joining with an electron or laser beam uses off set of the beam center to steel with the aim to melt only steel specimens and create a reactive interlayer with conduction heated titanium [3]. Another possible solution is using interlayers from metals, that have good weldability with titanium (zirconium, vanadium, niobium, molybdenum, tantalum, and

This work was presented at the conference Local Mechanical Properties 2022 held in Kosice, Slovakia on May 11-13, 2022.

Hana Chmelíčková, Vlastimil Jílek, Lukáš Václavek: Joint Laboratory of Optics of Palacký University and Institute of Physics AS CR, Faculty of Science, Palacký University in Olomouc, Joint Laboratory of Optics of Palacký University and Institute of Physics AS CR, Institute of Physics of the Academy of Sciences of the Czech Republic

Martina Havelková: Joint Laboratory of Optics of Palacký University and Institute of Physics AS CR, Institute of Physics of the Academy of Sciences of the Czech Republic

Aneta Hrubantová: Joint Laboratory of Optics of Palacký University and Institute of Physics AS CR, Faculty of Science, Palacký University in Olomouc, Department of Low-Temperature Plasma, Institute of Physics of the Czech Academy of Sciences

Tomáš Ingr: Department of Experimental Physics, Faculty of Science, Palacký University Olomouc

hafnium), but all of them are very expensive [4]. Solutions for mass production are using more accessible materials such as copper, nickel, and silver, that form with titanium less hard IMCs than Fe-Ti. Copper does not form intermetallic compounds with steel elements, its high ductility compensates difference in thermal expansion coefficients of Fe and Ti, but the strength of the joints strongly depends on various intermetallic phases in the Ti/Cu interface [5]. Known values of hardness are FeTi (~ 600 HV), Fe_2Ti (~ 1 000 HV), TiCu and Ti_2Cu_3 (998 HV – 1092 HV), Ti_2Cu (809 HV – 862 HV), Cu_4Ti_3 (917 HV – 973 HV), Cu_2Ti (408 HV – 537 HV) and Cu_4Ti (924 HV – 981 HV) [6]. The most promising method is using thin multilayers of the compatible metals with titanium (V or Nb) and Cu when the formation of Ti/Cu intermetallic is suppressed, but laser beam offset was revealed as the most critical parameter [7].

The majority of these cited experiments used butt weld configuration, the idea of our work is to examine lap joint arrangement with a thin bronze interlayer when the laser beam directly irradiates only the edge of the upper material and the other is melted or heated by thermal conduction. An influence of the pulse energy, an interlayer thickness, and the sheets' mutual position on the weld properties are tested. Inhomogeneous fusion zone properties are investigated by two microscopic methods, nanoindentation, SEM/ Energy Dispersive Spectroscopy, and X-ray diffractometry to reveal the location and amount of the intermetallic compounds.

MATERIALS AND METHODS

The austenitic stainless steel AISI 304 samples with a thickness of 0.6 mm and Ti6Al4V with a thickness of 1 mm were separated by bronze foil (CuSn6) 100 µm and 200 µm, resp. and fixed tightly on the welding jig in the lap configuration after brushing and cleaning with ethanol (Tab. 1). The laser beam in focus off set +3 mm has the theoretic diameter value 0.8 mm and it was centered to the steel upper edge with a tilt 15° from the vertical axis. Pulse frequency 13 Hz and linear axis speed 3 $mm.s^{-1}$ resulted in 70% laser spots overlap. High-purity argon was guided coaxial with a laser beam through a 2 mm nozzle with a flow rate of 12 $l.min^{-1}$. The pulse energy value was gradually set to 5.44 J, 5.58 J, 5.78 J, 5.87 J, 5.92 J, and 6.04 J, and the pulse length was set to a constant value of 3 ms, which was optimized in previous experiments. Then the mutual position of Ti6Al4V and AISI304 sheets was reversed and the experimental procedure was repeated with identical laser parameters, but the linear axis speed was set to 6 $mm.s^{-1}$ to reduce heat input to the specimen.

Tab. 1 Comparison of the selected thermo-mechanical properties of used welded materials, source https://matmatch.com/

Material	Density $kg.m^{-3}$	Hardness HV	Thermal expansion K^{-1}	Melting point K	Thermal conductivity $W.m^{-1}.K^{-1}$	Elastic modulus GPa
AISI 304	8 000	225 – 230	1.72 E^{-5}	1 728	12.2	193 – 200
Ti6Al4V	4 430	360 – 370	7.70 E^{-5}	1 947	6.7	114
CuSn6	8 820	80 – 120	1.80 E^{-5}	1 323	75	118

Weld macro-structure of the samples' transverse cross sections was observed using the laser scanning confocal microscope LEXT 5000 and the digital microscope KEYENCE VHX-7100. Three representative samples of each welding configuration were tested in the following methods, concretely sample T64_07 with 100 µm bronze interlayer (energy 5.58

J), T64_08 with 200 µm bronze interlayer (energy 5.87 J), and T64_04R with 100 µm bronze interlayer and reversed metal sheets position (energy 5.58 J). Nano-hardness tests of the main part of the inhomogeneous fusion zones surrounded by base materials were made using NanoTest NTX with pyramidal diamond Berkovich tip at a maximal load of 50 mN. The nanoindentation curves were evaluated by the Oliver-Pharr method for hardness and reduced elastic modulus determination. The indenter tip calibration was performed using the fused silica sample. Matrix's of (25 x 16) indents with spacing 30 µm were created and measured nanohardness values were displayed through the tables and graphs. To identify the chemical composition of the fusion zones, SEM/EDS analysis was done utilizing an SEM microscope Tescan VEGA 3 LMU. Data were displayed as EDS mapping both of the main elements Fe, Cu, and Ti and alloying elements Cr, Ni, Sn, Si, and Al too. EDS line spectra were measured in a diagonal direction across the fusion zone central part and horizontally in the interface region between the fusion zone and bottom specimen.
Intermetallic compounds Ti-Cu-Fe were characterized by X-ray diffractometry using Bragg-Brentano geometry. XRD analysis was performed on a D8 ADVANCE diffractometer (BRUKER) using Cu Kα radiation (λ = 0.154 nm) in the 2θ range 10°- 80°.

EXPERIMENTAL RESULTS AND DISCUSSION

Nanohardness test on the cross-section of the sample

The fusion zone of the sample T64_07 penetrates to titanium sheet with a maximum depth of 123 µm and a width of 443 µm at the interface level with CuSn6. Darker and lighter layers with different contents of welded metals steel and titanium alternate here due to melt pool flow. Copper is seen in the form of inclusions. The light grey region in the lowest part of the fusion zone probably contains IMC (Fig. 1(a)). Detail of this part shows copper droplets in probably a steel-rich region and a dark band of IMC on an interface with Ti6Al4V (Fig. 1(b)), where nanohardness values reached maxima from 8.18 GPa to 9.44 GPa.

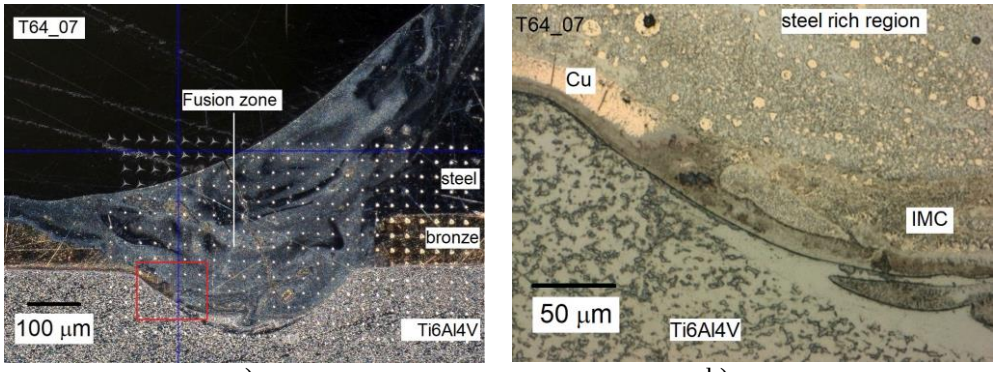

a) b)

Fig. 1. Cross section of the sample T64_07 with residual indents (a), (KEYENCE, mag. 200x); detail of the fusion zone on the bottom interface with Ti6Al4V (b), (LEXT, mag. 1200x).

Reduced elastic modulus (Er) distribution in the fusion zone of sample T64_07 was compared with the nanohardness graph (Fig. 2). There are seen individual bands of average modulus values 188 GPa, 120 GPa and 137 GPa on the right graph edge,

appropriate to the base materials steel, bronze and titanium alloy. Three regions with high modulus values from 184 GPa to 206 GPa occurred on the left edge of the fusion zone. The upper right part close to the bronze interlayer contains approx. 240 μm long band with module values from 182 GPa to 209 GPa (Fig. 2(a)). These high Er values mostly correspond with high nanonardness values (5.04 – 9.43) GPa and base materials positions, too (Fig. 2(b)).

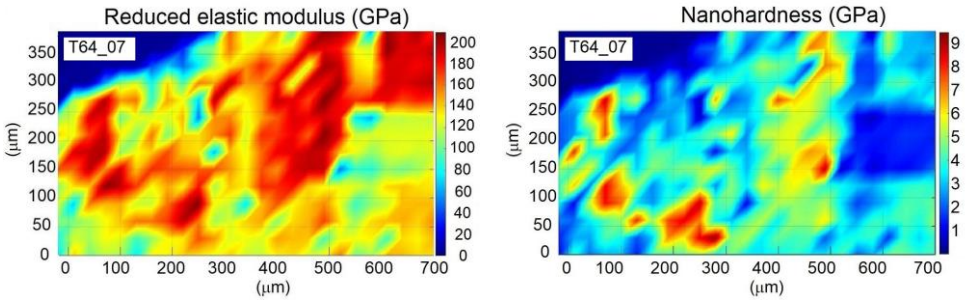

a) b)

Fig. 2. Comparison of the reduced elastic modulus distribution (a) and nanohardness distribution in the fusion zone of the sample T64_07 (b).

The fusion zone of the sample T64_08 penetrates the titanium sheet with a maximum depth of 137 μm and a width of 425 μm, measured with respect to the interface CuSn6/Ti6Al4V. Copper-rich regions prevail over mixed darker and lighter layers of Fe and Ti in the right, bottom, and upper left part of the fusion zone (Fig. 3(a)). The detail of this part is displayed in Fig. 3(b). The light grey steel-rich region with copper inclusion and copper-rich region with steel inclusions surround dark inclusion with titanium, high nanohardness values from 10.22 GPa to 10.96 GPa, measured in this region, point to the occurrence of IMC.

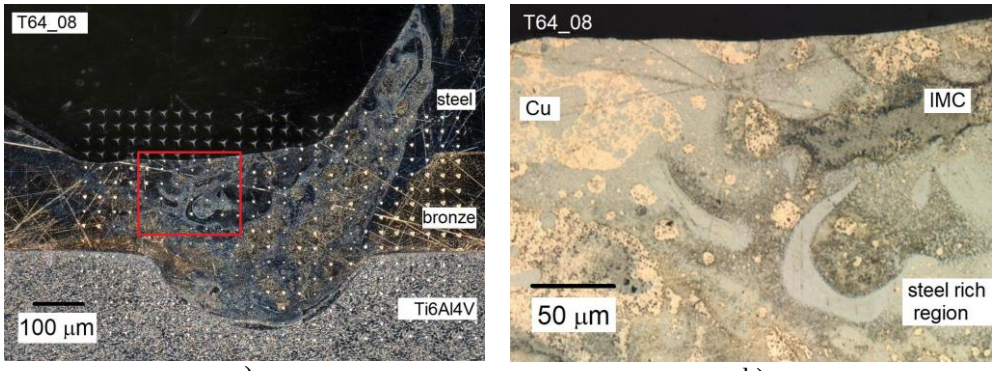

a) b)

Fig. 3. Cross section of the sample T64_08 with residual indents (a), (KEYENCE, mag. 200x); detail of the left upper part of the fusion zone (b), (LEXT, mag. 1200x).

Reduced elastic modulus (Er) distribution in the fusion zone of sample T64_08 was compared with the nanohardness graph (Fig. 4). Some blue islands with modulus

values from 25 GPa to 100 GPa are surrounded by the red range with high modulus values from 180 GPa to 228 GPa. Average values, measured behind the right edge of the fusion zone, correspond again with those of base materials, 184 GPa for steel, 125 GPa for bronze, and 137 GPa for titanium (Fig. 4(a)). The high nanohardness values from 8.03 GPa to 11.04 GPa in the left part of the fusion zone and on its interface with base materials steel and bronze correspond with high modulus values (Fig. 4(b)).

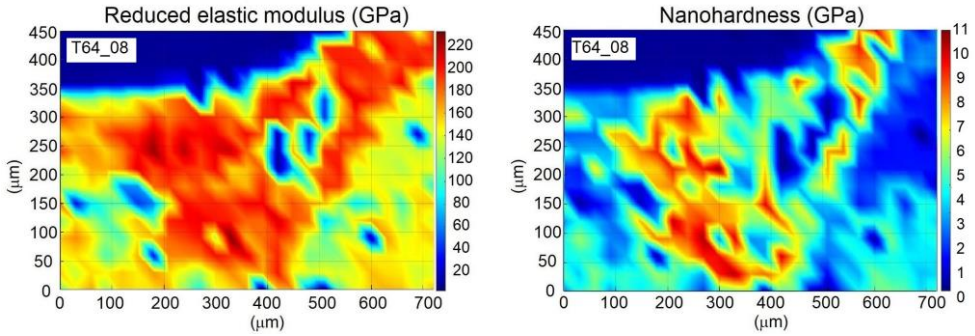

a) b)

Fig. 4. Comparison of the reduced elastic modulus distribution (a) and nanohardness distribution in the fusion zone of the sample T64_08 (b)

The influence of the higher welding speed and thus lower heat input on the welded materials mixing is seen on the cross-section of the sample T64_04R (Fig. 5(a)). Light grey regions with high content of the titanium are separated from the copper-rich dark region, a darker grey layered band is observable on the interface between the fusion zone and a bottom steel sheet. The detail of this part is displayed in Fig. 5(b). The copper-rich region with irregular titanium and steel scattered inclusions is surrounded by the dark band on the bottom interface with steel. The highest nanohardness values from 8.30 GPa to 9.63 GPa were measured in this region, which points to Fe–Ti intermetallic occurrence.

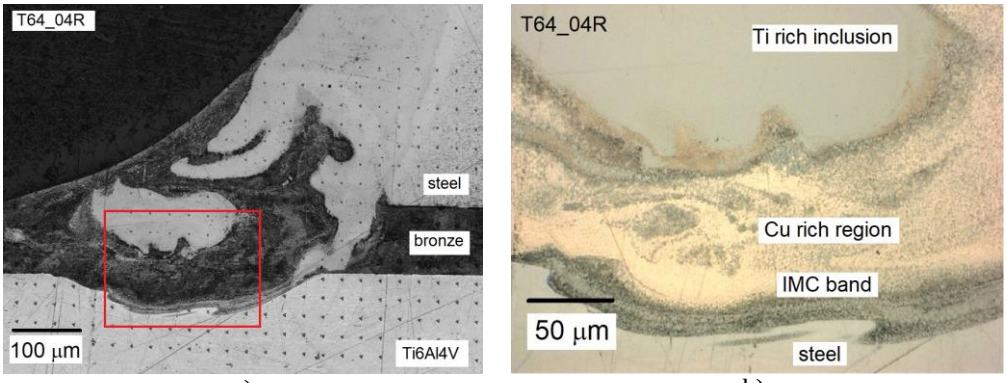

a) b)

Fig. 5. Cross section of the sample T64_04R with residual indents (a), (LEXT, mag. 432x); detail of the fusion zone on the bottom interface with steel (b), (LEXT, mag. 1200x)

Similarly, the reduced elastic modulus` distribution in the fusion zone of the sample T64_04R was compared with the nanohardness graph (Fig. 6). Average modulus values 134 GPa, 120 GPa, and 199 GPa on the right edge and bottom part of the graph belongs to above-mentioned base materials titanium alloy, bronze and steel, which are arranged in the reverse position against sample T64_07. The higher modulus values from 136 GPa to 191 GPa occurred in the left part of the fusion zone, they surround an area with values between 100 GPa and 120 GPa (Fig. 6(a)), where the titanium-rich island is seen in Fig. 5. The area of the same low modulus values is seen in the right upper part of the graph, where fusion zone borders on titanium alloy base material. The highest modulus values 226 GPa to 231 GPa are located in the bottom interface of the fusion zone with a steel metal sheet and correspond with the highest measured nanohardness values (8.30 – 9.63) GPa (Fig. 6(b)).

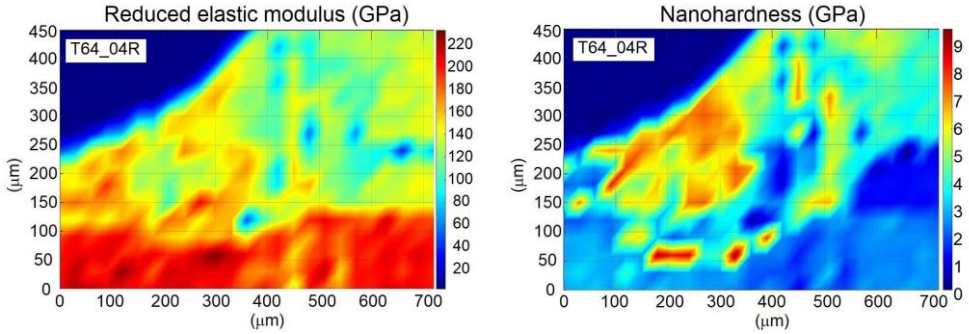

a) b)

Fig. 6. Comparison of the reduced elastic modulus distribution (a) and nanohardness distribution in the fusion zone of the sample T64_04R (b)

EDS mapping and line scanning, XRD analysis

The central fusion zone of sample T64_07 contains main steel elements Cr and Fe in the whole area with more intensive bands near the surface. Small, intensive islands of copper fill darker areas visible on Cr and Fe mapping. The original weak signal of titanium was lightened in the Fig. 7 to be observable mainly localized at the bottom of the fusion zone. Visible horizontal alternation of the steel-rich bands and bands with a higher copper content was caused by laser pulse overlap and repeated melting and convection of the fusion zone. Much larger separated copper-rich inclusions are observable in the case of sample T64_08 due to the twice thicker bronze interlayer. A more intensive titanium band is visible near the surface and bottom of the fusion zone (Fig. 8). Week signals of Cr and Fe are seen in the fusion zone of the sample T64_04R, where noticeably bounded areas of Cu and Ti are separated. The narrow band with high titanium content on the fusion zone bottom interface with the steel sheet is the location of the maximal nanohardness values (Fig. 9).

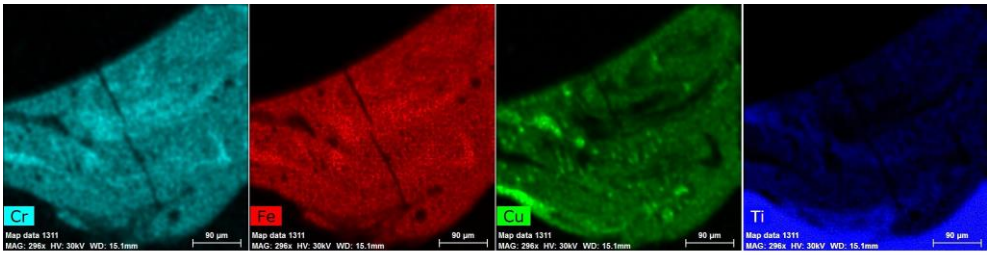

Map data 1311 MAG: 296x HV: 30kV WD: 15.1 mm scale 90 µm

Fig. 7. EDS mapping of the central fusion zone of the sample T64_07

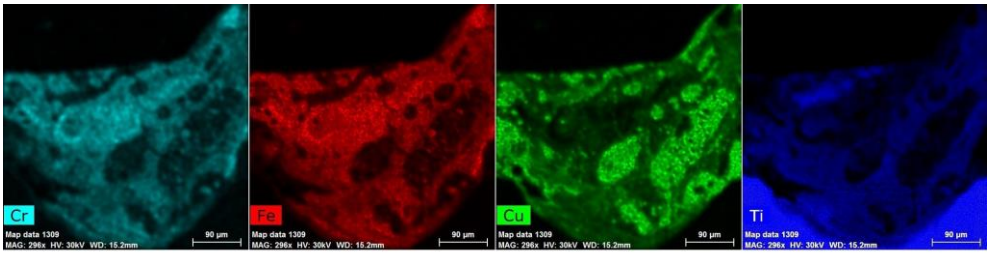

Map data 1309 MAG: 296x HV: 30kV WD: 15.2 mm scale 90 µm

Fig. 8. EDS mapping of the central fusion zone of the sample T64_08

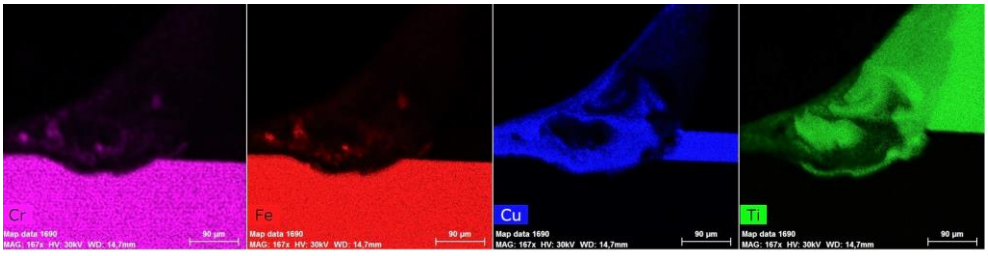

Map data 1690 MAG: 167x HV: 30kV WD: 14.7 mm scale 90 µm

Fig. 9. EDS mapping of the fusion zone of the sample T64_04R

The layered structure of the T64_07 fusion zone is documented by the signal variation of Fe, Ti, Cr, and Cu in the diagonal direction across its thickest part. Relatively high signal of titanium at positions about 265 µm and 370 µm proved melting of the bottom sheet interface and mixing it to the weld pool (Fig. 10(a)). XRD analysis detected two peaks (at 43° and 50°) of the solid-state solution Cu and Fe, quenched rapidly from the melt. At 43° and 50°, $Cu_{0.8}Fe_{0.2}$ (ISCD collection code 102894), was determined and is related to the (111) and (200) crystal planes, respectively. Intermetallic phase FeTi (ICSD collection code 633925) was determined at 43° and is related to the (110) crystal plane (Fig. 10(b)).

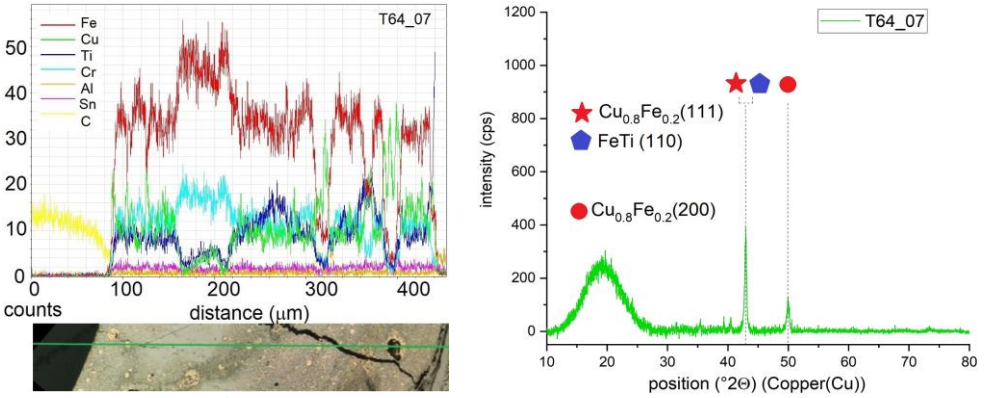

a) b)

Fig.10. EDS line scanning across T64_07 fusion zone in the diagonal direction (a); XRD diffractogram of the sample T64_07 fusion zone (b).

Alternation of the steel-rich and copper-rich regions in a sample T64_08 fusion zone is confirmed by Fe, Cr, and Cu counts` local maxima, EDS line scanning reveals higher signal of titanium at positions about 100 μm, 260 μm and 400 μm in the diagonal direction towards a bottom part of fusion zone (Fig. 11(a)). In a T64_08 sample fusion zone, peaks of α-titanium (ISCD collection code 253841), a solid solution of $Cu_{0.8}Fe_{0.2}$ (ICSD collection code 102894), and the intermetallic phase $CuTi_2$ (ICSD col. code 15807) were detected (Fig. 11(b)). The reflections occurred at 35.5°, 38.5°, 40.5, 53.2° and 63.6° are related to the (100), (002), (101), (102) and (110) crystal planes of α-titanium, respectively. The reflections from the $Cu_{0.8}Fe_{0.2}$ phase occur at peak positions 43.9° (111) and 50° (200). The reflections from the $CuTi_2$ phase subsist at peak positions 39.2° (102) and 43° (110).

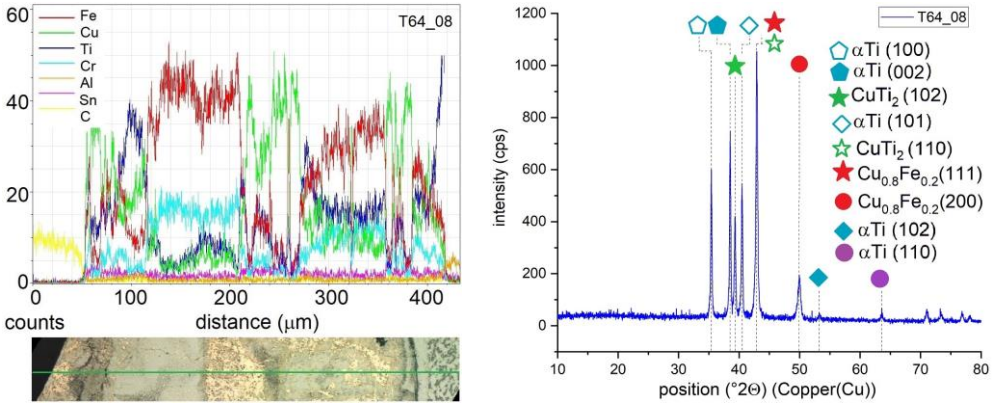

a) b)

Fig. 11. EDS line scanning across T64_08 fusion zone in the diagonal direction (a); XRD diffractogram of the sample T64_08 fusion zone (b)

EDS line scanning across the T64_04R fusion zone bottom part in the horizontal direction connected with adequate nanohardness values shows high titanium signal in the indents 9.2 GPa, 8.3 GPa, 8.7 GP, and 9.6 GPa (Fig. 12(a)). With the reverse arrangement of the lap weld with titanium sheet on top (sample T64_04R), two times less heat input and bronze interlayer of 0.1 mm, a spectrum of $Cu_{0.8}Fe_{0.2}$ (ICSD col. code 7954) and copper (ICSD col. code 7954) can be observed, the other phases only the α – titanium (ISCD col. code 253841) is presented (Fig. 12(b)). The reflections from the $Cu_{0.8}Fe_{0.2}$ phase occur at peak positions 42.9° (111) and 50° (200), we can also determine the Cu phase at peak positions 43.8° (111) and 50.9° (200), the origin of the peak with small intensity at position 40° should correspond with α – titanium (101). Although nanohardness values are high in certain areas and indicate the presence of IMCs, their peaks may not have been intense enough.

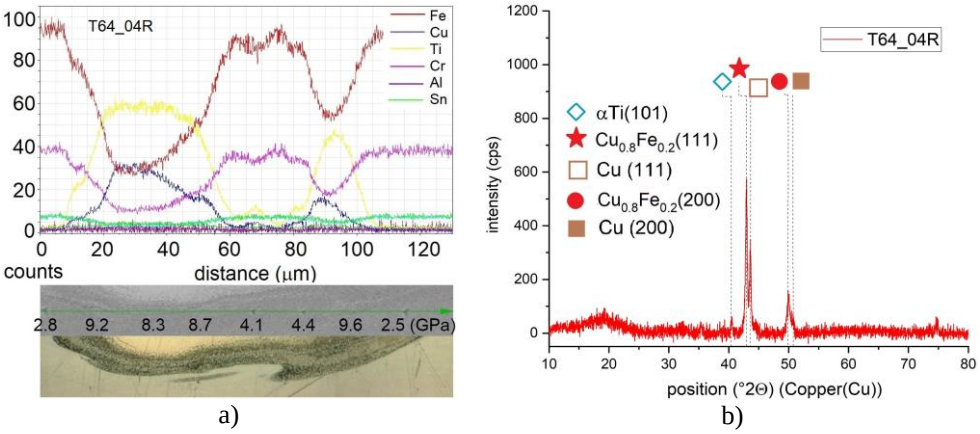

a) b)

Fig. 12. EDS line scanning across T64_04R fusion zone bottom part in the horizontal direction (a); XRD spectra of the sample T64_04R fusion zone (b)

CONCLUSIONS

Using a bronze interlayer with a thickness of 100 μm and 200 μm, lap welds of Ti6Al4V alloy (thickness 1 mm) and austenitic stainless steel AISI 304 (thickness 0.6 mm) were created in both arrangements of the sheet positions. From the results of performed analyses, it can be concluded that the fusion zone always contained a solid solution of iron and copper, quenched rapidly from the melt, and transformed titanium. In our experiment, the local occurrence of intermetallic phases was dependent on the thickness of the interlayer and the heat input, which decreases proportionally with the increasing welding speed. Large overlapping pulses, repeated melting, and extensive melt flow resulted in the mixing of materials and intermetallic compounds formation in the fusion zone, which caused cracks.

In the case of 100 μm interlayer and heat input 24.18 $J.mm^{-1}$, areas with higher content of FeTi had much higher nanohardness and reduced elastic modulus than basic material with values higher than 9 GPa respectively 200 GPa. With a higher content of copper in the fusion zone in the case of 200 μm interlayer and heat input 25.44 $J.mm^{-1}$, distinguishable areas rich in either copper or iron were formed and the intermetallic $CuTi_2$ prevailing over FeTi were detected. Maxima of nanohardness and reduced elastic modulus are higher than 11 GPa, respectively 220 GPa.

At a higher velocity and lower heat input of 12.09 J.mm^{-1}, we observe the change in the layout of areas with similar values of nanohardness and reduced elastic modulus. It shows the permeation of the noticeably bounded areas with a predominance of titanium or copper, corresponding nanohardness and elastic modulus values are less than in previously mentioned cases. The highest values were measured only on the fusion zone interface with Ti6Al4V base material.

The fusion zone depth and internal microdefects depend not only on the laser parameters and heat input, but an important parameter is also on the inclination of the laser head and focus of the laser beam against the edge of the upper sheet. The lower sheet has to be melted to a minimal depth to limit greater penetration of its elements into the melt pool.

It has been demonstrated that with the proper setup is it possible to create a lap weld without surface cracks between otherwise incompatible materials AISI 304 and Ti6Al4V using a thin bronze interlayer.

ACKNOWLEDGMENT

The research work reported here was made possible by the continuous support of the Operational Program Research, Development, and Education, project no. CZ.02.01/0.0/0.0/17_049/0008422 of the Ministry of Education, Youth and Sports of the Czech Republic.

REFERENCES

[1] Chen, S., Zhang, M., Huang, J., Cui, C., Zhang, H., Zhao, X.: Materi. Des., vol. 53, 2014, p. 510.
[2] Tomashchuk, I., Sallamand, P.: Adv. Eng. Mater., vol. 20, 2018, p. 4.
[3] Mannucci, A., Tomashchuk, I., Mathieu, A., Cicala, E., Boucheron, T., Bolotl, R., Lafaye, S.: Procedia CIRP, vol.74, 2018, p. 490.
[4] Zhang, Y., Sun, D., Gu X., Li, H.: Mater. Lett., vol. 185, 2016, p. 152–155.
[5] Tomashchuk, I., Sallamand, P., Andrzejewski, H., Grevey, D.: Intermetallics, vol. 19, 2011, p. 1466.
[6] Mitelea, I., Groza, C., Craciunescu, C.: J. of Materi Eng and Perform, vol. 22, 2013, p. 2220.
[7] Li, J., Liu, Y., Gao, Y., Jin, P., Sun, Q., Feng, J.: Opt. Laser Technol., vol. 125, 2020, p. 8.

sciendo Powder Metallurgy Progress, Vol.22 (2022), No.1, p.053-061
http://dx.doi.org/10.2478/pmp-2022-0007

THE INFLUENCE OF TILT ON BERKOVICH INDENTATION OF A STEEL SAMPLE USING FEM ANALYSIS AND NANOINDENTATION

Jaroslav Kovář, Vladimír Fuis, Radim Čtvrtlík, Jan Tomáštík

Abstract
The main shape deviations of a Berkovich indenter are the indenter bluntness and indenter tilt. The influence of the Berkovich indenter tilt on the results of the FEM modelling of steel nanoindentation is evaluated in this paper. The indenter tilt has an impact on the indentation curves and contact area. The X5CrNiCuNb 16-4 steel nanoindentation was modelled by FEM and the indentation curves were obtained. The Berkovich indenter was blunted and the tilt of the indenter was changed to determine its influence on the indentation curves. The results showed that growing tilt shifts the indentation curves to higher values of indentation forces and makes unloading curves steeper which is in agreement with a larger contact area. The calculated indentation curves were compared with the experimental indentation curves and the impact of the indenter tilt to the indentation curves was determined.
Keywords: nanoindentation, indenter shape deviations, indenter tilt, indenter bluntness

INTRODUCTION

Nanoindentation test

The nanoindentation test is often used to determine the Young modulus and hardness of the bulk materials or thin layers. At this test, the indenter is pressed into the specimen and the dependency of the indentation force on the indenter displacement (indentation curve) is measured. The Young modulus and hardness can be obtained from the indentation curve using the Oliver-Pharr analysis [1].

To perform the Oliver-Pharr analysis, the indentation curve and the indenter shape function have to be known. It is the dependency of the projected contact area (A_c) on the depth of the indentation without sink-in effect (h_c). The indenter shape function for the ideal indenter can be calculated by (1).

$$A_c = 24.56 \cdot h_c^2 \tag{1}$$

The indenter shape function determined by (1) is usually not enough accurate to describe the contact area when the experiment is done. The main reasons are the shape deviations of the indenter and the surface of the specimen and the pile-up effect [2].

This work was presented at the conference Local Mechanical Properties 2022 held in Kosice, Slovakia on May 11-13, 2022.
Jaroslav Kovář, Vladimír Fuis: Institute of Solid Mechanics, Mechatronics and Biomechanics, Brno University of Technology, Brno, Czech Republic
Vladimír Fuis: Centre of Mechatronics, Institute of Thermomechanics of the Czech Academy of Sciences, branch Brno, Czech Republic
Radim Čtvrtlík, Jan Tomáštík: Institute of Physics of the Czech Academy of Sciences, Joint Laboratory of Optics of Palacky University Olomouc and Institute of Physics of the AS, Czech Republic

At the nanoindentation, the surface near the indenter can bend under the indenter and then the projected contact area gets smaller, this is called the sink-in effect. The sink-in effect is included in the commonly used Oliver-Pharr analysis. If the plasticity of the specimen is huge, then the plastically deformed material accumulates under the indenter and creates a pile-up region. The pile-up makes the contact area bigger and it needs to be corrected to get correct results of Young's modulus or hardness [3].

FEM modelling of the nanoindentation test

The modelling with FEM can be used to study the results and the influences of the nanoindentation test without preparing the specimens and measurements. The FEM can be used to determine the contact pressure, the strain and stress fields under the indenter, and the border of the pile-up region. The FEM was used to calculate the correction factor β for the conical and Berkovich indenter [4] and can be inversely used to determine the parameters of the model of material from known indentation curves [5]. With the help of FEM, the influences of the indenter bluntness [6] and specimen tilt can be studied.

The impact of shape deviations

The shape deviations are crucial to the determination of the correct value of the projected contact area. The bluntness of the indenter has the highest impact on the results. The growing bluntness makes the contact area bigger and it needs to be included in the indenter shape functions, which is determined at the calibration [1]. When the FEM modelling is used with the ideal shape of the indenter, there is no calibration and then the indentation curves have different shapes but the determined values of the Young modulus are the same. The impact of the indenter bluntness on the indentation curves was determined in [6].

Another shape deviation is the mutual tilt of the indenter and specimen. Although the tilt is included in the shape function at calibration too, the measurement is done on another specimen, whose surface has a different tilt than the specimen with the reference material. This tilt influences the contact area [7] and it can influence the indentation curves too. The main aim of this work is the determination of the indenter tilt influence on the indentation curves. The influence of the indenter tilt in the plane of symmetry will be determined and then the plane of tilt will be rotated to check the influence of tilt in another axis. The effect of indenter tilt was determined for fused silica, which has sink-in behavior [7] but not for materials with pile-up as steel, which will be the main aim in this paper.

METHODS

Model of material

The indentation of the X5CrNiCuNb 16-4 steel was experimentally measured and the same material was expected for the FEM modelling. To get a precise description of the behavior of this material, the tensile test was done (Fig. 1) and then it was modelled by FEM to calibrate the model of the material.

The stress-strain curve of the steel (Fig. 2) is composed of three parts. The first part is the linear-elastic model of the material. Young's modulus was used from the experimental measurement (E_s = 202 GPa). The Poisson's ratio was not measured but a commonly used value ($\nu = 0.3$) was used.

The second part of the steel stress-strain curve starts with the first plastic deformation. The multilinear elasto-plastic model with isotropic hardening was used to describe the stress-strain curve by eleven points on its and connected by lines (Fig. 2). To get the most precise results, the first point of the multilinear elasto-plastic model was

placed at a point, where the start of deviation from the line in the experimentally measured stress-strain curve was apparent. At this part, the few points of the multilinear model were fitted to experimentally measure the stress-strain curve. This curve can be used until the reach of the ultimate strength. At this point, the experimentally measured stress-strain curve is not valid anymore due to the start of necking When necking occurs, the plastic deformation starts to localize in the small area in the specimen center and the measured stress-strain curve cannot be used for the model of material for FEM anymore.

To describe the part of the stress-strain curve after necking, the FEM model of the tensile test was done. The small imperfection was added to the FEM model to get the neck in the center of the specimen. With this model, the FEM simulation of the tensile test with necking was calculated. A few other points were added to the stress-strain curve and their values were iteratively changed to get the same force-displacement curve as was measured by the tensile test. The necking was included in the FEM model and then it was comparable with the experimental measurement (Fig. 1). The calculated curves gave great conformity with the experimental force-displacement curve from the tensile test and then determined points could be added to the model of material (Fig. 2).

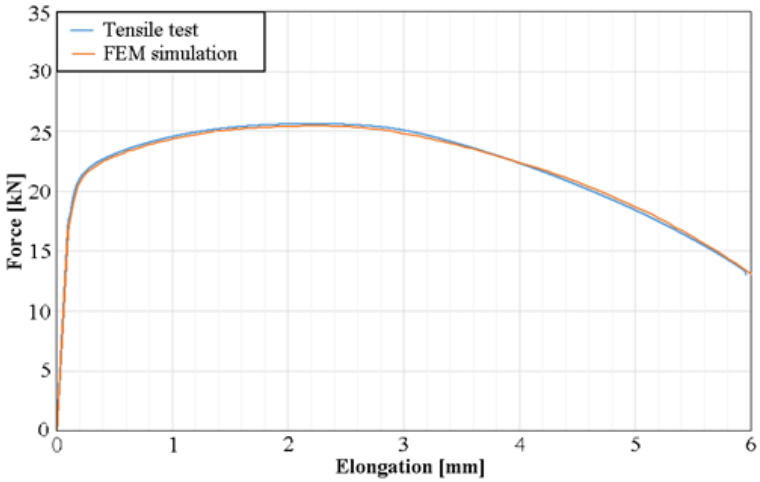

Fig. 1. Comparison of the tensile test results and the force-elongation curve calculated by FEM.

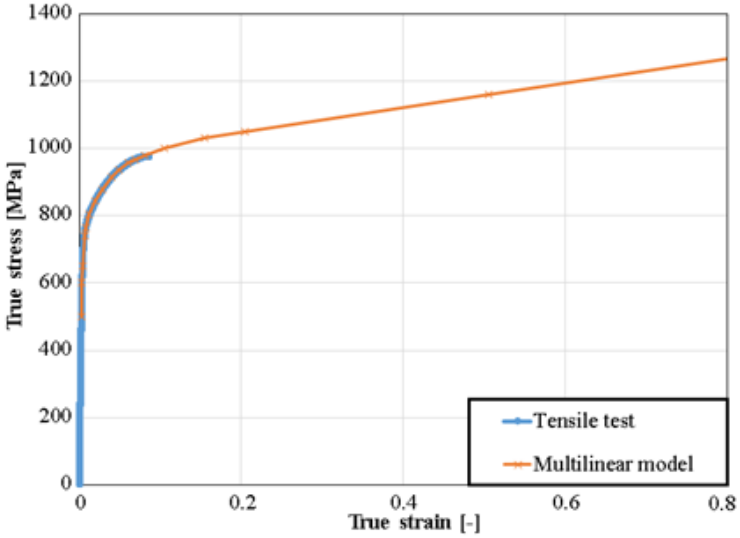

Fig. 2. The calculated parameters of the model of material, subsequently used for the modelling of the nanoindentation test.

FEM model of indentation with blunted indenter

Model of geometry – The geometry of the specimen and modified Berkovich indenter (referred to as Berkovich indenter) was created. The dimensions (Fig. 3) were chosen to be at least 100 times bigger than the depth of indentation, to prevent the influence of the results by the edge of the specimen. The Berkovich indenter was expected as blunted. The bluntness of 400 nm was applied to its tip and edges. This bluntness was chosen to be slightly lower than is allowed by ISO 14577-1. [8], where the bluntness of 500 nm is allowed for the used depths of indentation. The bluntness is shifting the indentation curves to the higher values of forces and can have a significant impact on the results [6]. The blunted Berkovich indenter has three planes of symmetry and due to the symmetry of the geometry, material, boundary conditions, and expected symmetry of the results, only one sixth of the indenter and specimen was modelled.

Boundary conditions – Due to the symmetry, the displacement perpendicular to the planes of symmetry was fixed on the areas in the planes of symmetry. The displacement in the way of z axis was fixed on the lower area of the specimen (Fig. 3). The specimen was loaded by the displacement of the Berkovich indenter. The loading was divided into two load steps. In the first load step, the displacement of 500 nm plus the gap between the specimen and the blunted indenter, caused by the bluntness, was applied on the upper area of the indenter. In the second load step, the indenter was moved back to separate the indenter and specimen. The large displacements were expected and the loading and unloading phase were divided into more than 100 substeps.

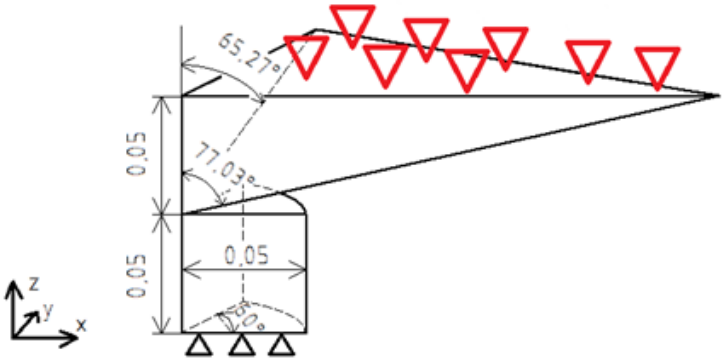

Fig. 3. The geometry and boundary conditions used for FEM.

Mesh – The mesh (Fig. 4) was created from the volume elements with quadratic base functions (SOLID 186). The mesh was from hexaedrical coarse elements far away from the contact region and very fine elements under the indenter. The transitional volume from tetraedrical elements was created between these two volumes. The indenter was meshed with elements with tetraedrical shape, which were fine on the tip of the indenter and coarse in the far volume. The contact region was created between the specimen and indenter and meshed with the CONTA 174 and TARGE 170 elements. The surface of the specimen was chosen as a contact area and the surface of the indenter as a target. The factor of penetration tolerance was lowered to get the penetration lower than 1 nm. The steel has a pile-up behavior and then the coefficient of friction needs to be used between the indenter and specimen. The value of $\mu = 0.1$ was assumed [9].

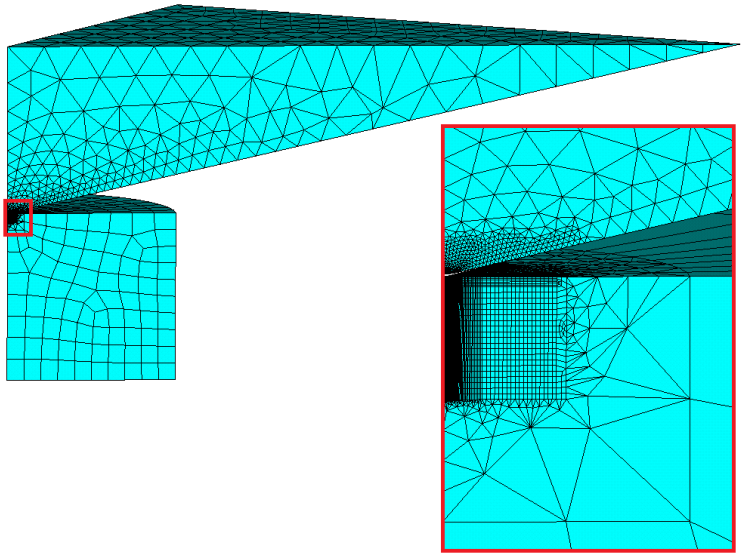

Fig. 4. Mesh used for FEM calculations.

FEM model of indentation with blunted indenter and tilted specimen

To calculate indentation curves for the tilted specimen, the FEM model was modified. The specimen was tilted in the plane, which includes the edge of the Berkovich indenter (Fig. 5). The tilt was chosen from 1° to 5° with the step of 1°. Due to the tilt of the specimen, there are not three planes of symmetry anymore. Only one plane of symmetry, which is the same as the plane of the tilt, left; therefore, half of the model was modelled. The displacements perpendicular to this plane were fixed on it and the displacement in the x-axis needed to be fixed on the lower area of the specimen and the upper area of the indenter. It was verified that these changes do not influence the results of the calculations.

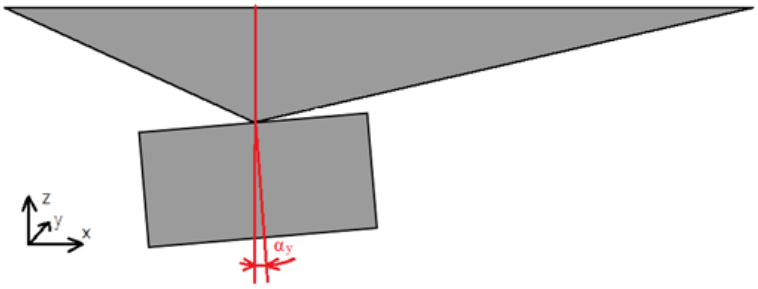

Fig. 5. Indentation with tilted specimen.

FEM model of indentation with rotated plane of tilt

The specimen tilt is often general; therefore, the tilt plane does not have to be the plane with the edge of the indenter. To check the influence of the indenter tilt plane, the plane of the tilt was rotated from 0° to 60° with the step of 20°, and the FEM calculations were done. The rotation of about 60° was calculated with the same model as was used for the tilting in the plane with the edge of the indenter, only the tilt was done in the opposite direction. To calculate two other cases (rotation of the tilting plane about 20° and 40°), the full model needed to be done. The displacement in all directions was fixed on the lower area of the specimen and displacement in the x and y axes were fixed on the upper areas of the indenter. In this case, the computational time grew up a lot. To make the task be calculated in less than 5 days, the mesh had to be coarser. It could slightly influence the accuracy of the calculated contact pressures, which were not evaluated, but the displacements and forces, which are less sensitive to mesh quality should be accurate enough, so the change of mesh should not significantly influence the calculated indentation curves.

RESULTS AND DISCUSSION

The influence of the indenter tilt

The first calculations were made with the blunted Berkovich indenter without the tilt of the specimen. The calculated indentation curves (Fig. 6) showed lower values of the indentation forces than experimental data. This can be caused by either higher bluntness than was expected in the calculation [6] or by the tilt of the indenter.

The results of FEM calculations show higher values of indentation forces with growing tilt. The difference in the curves caused by the 1° tilt is getting bigger with the growing specimen tilt. At the tilt of 5°, the calculated loading curves show great correlation with the experimental data. The unloading curves fit experimental data well in the first half of unloading. There is a discrepancy in the last phase of unloading, which can be caused by

the more complex plastic deformation caused by the residual stresses. This discrepancy should not influence the commonly used Oliver-Pharr analysis, because, the only first part of the unloading curve is usually used.

The growing values of the maximal force and slightly growing unloading stiffness are in agreement with [7]. In this paper, the indenter shape function for the ideal tilted indenter was analyzed with the result that the contact area is growing with the tilted specimen. To get the correct value of Young's modulus, the higher values of the indenter shape function are related to the steeper unloading curve.

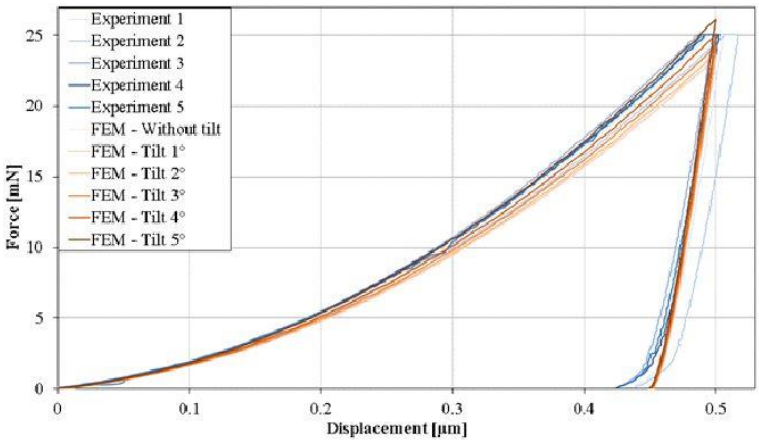

Fig. 6. Comparison of the indentation curves calculated for the different indenter tilts with the experimentally determined indentation curves.

The influence of the rotation of the tilt plane

After the determination of the influence of the specimen tilt in the plane of the edge of the specimen, the calculations with the rotated plane of the specimen tilt were calculated and the influence of the direction of the tilt was determined. The calculated indentation curves for the tilt of 5° in the plane rotated about 0°, 20°, 40°, and 60° were compared (Fig. 7). Due to the geometry of the indenter and the specimen, higher angles of the rotation of the tilt plane are symmetrical with calculated results.

The indentation curves show that the rotating of the specimen tilt plane influences results only slightly. When the tilt is in the plane of the indenter edge or rotated by 10°, the indentation curves have nearly the same results. With the growing rotation of the tilt plane, the maximal values of the forces slightly decrease. The biggest difference is for the tilt plane in the center of the indenter side surface (opposite tilt to the indenter edge). The relative difference to the tilt in the 0° plane is 3 %. The results show that the rotation of the plane of indenter tilt has a smaller influence on the results opposite to the angle of indenter tilt or indenter bluntness [6].

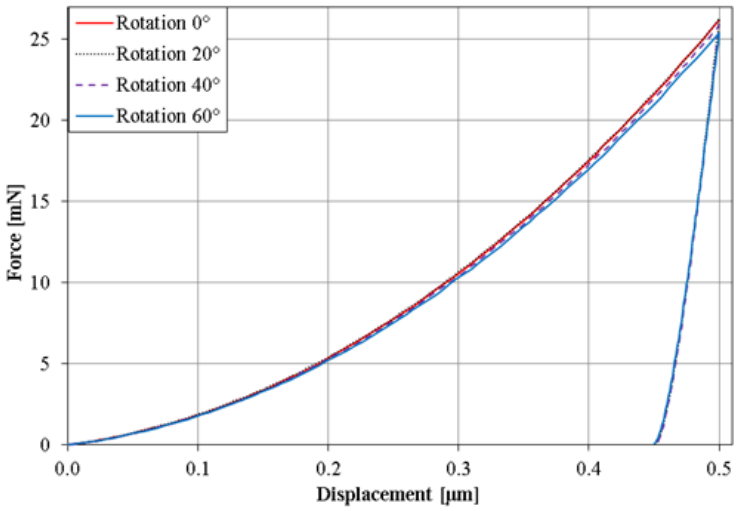

Fig. 7. Calculated indentation curves with the 5° tilt of specimen and rotated tilt plane.

The Young's modulus and hardness

To determine the Young's modulus and hardness, the Oliver-Pharr analysis [1] was used. Due to the pile-up, the experimental results were distorted, due to the inability to measure the correct value of the projection of the contact area. For the results obtained by FEM, the contact area was determined from the surface of the elements in contact projected to the plane of the specimen surface. The correction factor for the influence of radial displacements $\beta = 1.06$ [10, 11] was used. The calculated value of reduced modulus for the indentation without tilt was 191 GPa, which was the same as for the indenter with 5° tilt. When the rotation of the tilt plane at about 60° occurred, the determinated reduced modulus dropped to 186 GPa. Similar results were obtained for hardness, which was 3.0 GPa for the indenter without tilt, 3.1 GPa for 5° tilt, and 3.1 for the rotated plane of the tilt. The calculated reduced modulus 191 GPa matches with the specimen Young's modulus 204 GPa, which is nearly the same as the value measured from the tensile test and used for FEM calculations which was 202 GPa. All calculated results show that the indenter tilt does not have any significant impact on the determined values of Young's modulus and hardness if the contact area is correctly determined.

CONCLUSIONS

The influence of the indenter tilt on the indentation curves was analyzed in this paper. The model of material of X5CrNiCuNb 16-4 steel was fitted to experimental data and verified by FEM and then used for the FEM calculation of the nanoindentation with the blunted and tilted indenter. The growing indenter tilt makes higher indentation forces. This is in agreement with [7] which shows higher contact surfaces caused by the indenter tilt. At the nanoindentation test, the specimen is tilted in a random direction. To analyze this influence, the full model of the indenter and specimen was done, and the tilt plane was rotated from 0° to 60° with step 20°. The higher angles of tilt plane rotation are symmetrical with the calculated results. The results show that there is only a small difference in the indentation curves with the rotating tilt plane. In our previous paper [6], the influence of the indenter bluntness on the indentation curves was analyzed. The

comparison of all influences indicates that the most important influence on nanoindentation is caused by the indenter bluntness. The tilt could have a significant impact on the indentation curves but if the contact area is corrected, the calculated Young's modulus and hardness are not influenced. The influence of the tilt plane rotation is not so much important and usually can be omitted from another FEM calculation. This is important because the symmetry can be used to reduce the model and save computational time.

ACKNOWLEDGMENT

The tensile test was measured by the Institute of Material Sciences and Engineering of the Faculty of Mechanical Engineering, Brno University of Technology.

This study was realized with the support by the grant FSI-S-17-4386 and with the institutional support RVO: 61388998.

Computational resources were supplied by the project "e-Infrastruktura CZ" (e-INFRA CZ LM2018140) supported by the Ministry of Education, Youth and Sports of the Czech Republic.

The authors also gratefully acknowledge the support by the Operational Program Research, Development and Education, projects No. CZ.02.1.01/0.0/0.0/17_049/0008422 and No. CZ.02.1.01/0.0/0.0/16_019/0000754 of the Ministry of Education, Youth and Sports of the Czech Republic. R.C. and J.T. also thank the project No. TN01000038 of the Technology Agency of the Czech Republic for support of their workplace.

REFERENCES

[1] Oliver, W. C, Pharr, G. M.: Journal of Materials Research, vol. 7, no. 6, 1992, p. 1564.
[2] Oliver, W. C, Pharr, G. M.: Journal of Materials Research, vol. 19, no. 1, 2004.
[3] Kese, K., Li, Z. C. In: Scripta Materialia, vol. 55, no. 8, 2006, p. 699.
[4] Shim, S., Oliver, W. C, Pharr, G. M.: International Journal of Surface Science and Engineering, vol. 1, no. 2/3, 2007, p. 1749.
[5] Kovář, J., Fuis, V.: Engineering Mechanics 2019, Svratka, Czech Republic, 2019, p. 189.
[6] Kovář, J., Fuis, V., Tomáštík, J.: Acta Polytechnica CTU Proceedings, Prague, Czech Republic, 2020, p. 131.
[7] Shi, C., Zhao, H., Huang, H., Xu, L., Ren, L., et al.: Materials Transactions, vol. 54, no. 6, 2013, p. 958.
[8] ISO 14577-1:2015, 2015.
[9] Kovář, J., Fuis, V., Čtvrtlík, R.: ENGINEERING MECHANICS 2020, Brno, Czech Republic, 2020, p. 298.
[10] Hay, J. C., Bolshakov, A., Pharr, G. M.: Journal of Materials Research, vol. 14, no. 6, 1999, p. 2296-2305.
[11] Kovář, J., Fuis, V., Čtvrtlík, R., Tomáštík, J.: Journal of Materials Research vol. 37, no. 10, 2022, p. 1750.

Powder Metallurgy Progress, Vol.22 (2022), No.1, p.062-074
http://dx.doi.org/10.2478/pmp-2022-0008

EFFECT OF MACHINING ON MECHANICAL PROPERTIES OF BOROSILICATE GLASSES

Lukáš Václavek, Jan Tomáštík, Radim Čtvrtlík

Abstract

Although optical properties are essential for materials for optical purposes, their mechanical properties must also be considered as they directly govern their practical applicability as well as their machining. The machining of optical glasses is mainly carried out by mechanical removal of the material using free or bonded abrasives. The relationship between the local mechanical properties of three types of borosilicate glasses used to produce optical elements (mirrors) and the type of surface machining was investigated. The samples were machined using two approaches, namely 7-axis CNC surface machining and conventional manual machining. Advanced analysis of nano/micro-mechanical properties was performed on glass samples using quasi-static nanoindentation and microindentation and dynamic impact test complemented by the analysis of the acoustic emission signals generated during the mechanical tests.

The results show a difference in mechanical properties between industrial and optical borosilicate glasses. The type of machining has a strong influence on studied mechanical properties and surface quality. Glasses manufactured by CNC have more pronounced acoustic emission signal and crack more than glasses manufactured by hand. The different behavior of hand- and CNC-machined surfaces can be linked to different subsurface damage caused by different contact conditions between the workpiece and the instrument/abrasive. As a result, a different density of surface and especially (near)-subsurface flaws are present in the glass. Simax is slightly softer than BG33 glass, which together with the less pronounced AE may indicate a lower amount of subsurface cracks/damage.

Keywords: borosilicate glass, mechanical properties, indentation, acoustic emission, glass manufacturing

INTRODUCTION

The optical devices inherently rely on the superior optical performance of individual elements. However, for practical applications, the mechanical properties of these materials must also be taken into consideration.

This work was presented at the conference Local Mechanical Properties 2022 held in Kosice, Slovakia on May 11-13, 2022.

Lukáš Václavek, Jan Tomáštík, Radim Čtvrtlík: Palacký University in Olomouc, Faculty of Science, Joint Laboratory of Optics of Palacký University and Institute of Physics AS CR, 17. Listopadu 12, 771 46 Olomouc, Czech Republic

Lukáš Václavek, Jan Tomáštík: Institute of Physics of the Czech Academy of Sciences, Joint Laboratory of Optics of Palacky University and Institute of Physics AS CR, 17. Listopadu 50a, 772 07 Olomouc, Czech Republic

This is especially crucial for the design optimization and lifetime estimation of optical components as well as for their manufacturing. In this context, the issue of surface machining quality is of particular importance. Machining based on the mechanical removal of the material is a multiparametric process, and its optimization is vital for achieving superior surface quality.

For large optical assemblies, such as fluorescence telescopes (Pierre Auger Observatory, Cherenkov Telescope Array, Fluorescence detector Array of Single-pixel Telescopes), borosilicate class of glasses is used with advantage due to its mechanical, chemical, and thermal stability. In this respect, especially coefficient of thermal expansion is very low and plays a crucial role for this application. Borosilicate glasses are a low-cost compromise of glass with very low coefficient of thermal expansion and good mechanical and optical properties for this type of application. By definition, borosilicate glass contains B_2O_3>8% and is characterized by high strength and resistance to deformation and fracture, also it exhibits relatively high values of Young modulus and hardness in comparison to other types of glasses [1].

The surface quality of optical elements is one of the most important characteristics vital for their successful application. In this respect, the technology of surface grinding and polishing plays a crucial role in determining the surface roughness and subsurface damage. It is clear that for evaluation of the material surface quality, the appropriate techniques reflecting the local character must be used. Nano and microindentation techniques have proved to be very useful techniques for the evaluation of surface and mechanical quality of glass surfaces [2, 3]. This study deals with the local mechanical testing of three types of borosilicate glasses used for the production of optical elements, especially mirrors. The relationship between two types of surface machining, CNC (Computer Numeric Control) surface machining and conventional freehand machining (hand grinding and polishing), and the mechanical properties and the surface quality were studied. Advanced analysis of nano/micro-mechanical properties was performed on glass samples using quasi-static nanoindentation, microindentation, and dynamic impact test. During the mechanical tests, acoustic emission (AE) signals were continuously acquired to detect subsurface disturbances and cracking.

MATERIALS AND METHODS

Sample preparation

Two types of industrial glasses: i) Simax glass from the KAVALIERGLASS, a.s. (Sázava, Czechia), ii) Borosilicate Float Glass 3.3 (BG33) from a JINAN GT INDUSTRIAL CO., LTD (Jinan, China) and a reference optical glass iii) BK7 from Schott AG (Mainz, Germany) as a typical representative of optical borosilicate glass used for the production of optical elements were explored. The overview of the investigated glasses including their chemical composition is shown in Tab. 1. Two series of circular samples with a diameter of 15 mm and a thickness of 4 mm from each type of glass were prepared in the first step. Subsequently, one group of samples was machined by hand machining and the second group of samples was machined by a 7-axis CNC machine. The manual machining of the measured area was carried out by grinding (final grinding with Al_2O_3 F800 abrasive) and polishing with a Cerox 1670 polishing resin tool for 2 hours. CNC machining samples were machined using the sub-aperture CNC machining method in two successive steps. The first step consisted of grinding with a diamond pot mill resulting in the desired plane shape. The grinding was carried out in several steps to eliminate subsurface cracking and to allow polishing of the glass surface in subsequent steps. The

grinding was carried out using a tool with abrasive material (diamond grains) bonded to a solid material (brass, resin), with the removal function being entirely dependent on the position of the tool. In contrast, the polishing was done with a tool in the form of hollow elastic material, which can be pressurized with air and thus its hardness can be controlled and has the function as an abrasive carrier so that the removal function is most dependent on the processing time at that location and air pressure in this tool.

Tab. 1 Sample overview

Sample	Type of glass	Chemical composition	Machining	
			CNC	Hand
BK7 BK7 CNC	Borosilicate	SiO_2 69.13%; B_2O_3 10.75%; BaO 3.07%; Na_2O 10.40%; K_2O 6.29%; As_2O_3 0.36%	✓	✓
BG 33 BG33 CNC	Borosilicate	SiO_2 80%; B_2O_3 13%; Al_2O 2%; Na_2O 4%; K_2O 1%	✓	✓
Simax Simax CNC	Borosilicate	SiO_2 80.3%; B_2O_3 13.0%; Al_2O_3 2.4%; Na_2O + K_2O 4.3%	✓	✓

Mechanical properties:

Mechanical properties were measured using the fully calibrated NanoTest instrument via a comprehensive set of techniques, including nanoindentation, microindentation, and dynamic impact tests. The nanoindentation test was carried out by the Berkovich indenter at different loads, loading rates, and time courses (load-creep-unload). Measurement at 10 mN and a time course of 10-10-10 s (load-creep-unload) was used to measure mechanical properties such as hardness, modulus of elasticity, and W_p/W_t ratio. Further measurements at loads of 100, 250, and 500 mN during a time course of 20-20-20 seconds were applied to measure indentation-induced cracking. The indentation-induced cracking was measured using microindentation with maximum load force 1, 5, 10, and 20 N with Berkovich indenter during a time schedule of 20-20-20 seconds. The dynamic impulse test is handled to simulate repeated deformation in operating conditions. This test was performed by a spherical indenter with a tip radius of 10 μm and a maximum load of 10 mN, the number of repetitions was 75 times, the total time was 300 seconds and the on-load/rest period was 2/2 seconds. Simultaneous detection of acoustic emissions (AE) [4] has been carried out during all tests to detect elastic waves triggered by the deformation and failure of the material. A dedicated sample holder with a built-in piezo sensor and preamplifier with high sensitivity and low noise was handled for AE detection. The evaluation of the AE signal, sampled at the sampling frequency of 10 MHz and processed with a 16-bit control and processing unit, was performed via a ZEDO Daemon software.

EXPERIMENTAL RESULTS AND DISCUSSION

Nanoindentation

The results of the nanoindentation measurement performed at a maximum force of 10 mN was calculated via the O-P method [5] and are summarized in Fig. 1. It can be clearly seen that the BK7 glass samples, both hand and CNC machined, are close to the tabulated values declared by the manufacturer (Young's modulus of 82 GPa corresponding to reduced modulus of 85.6 GPa, Poisson's number of 0.206 [6]). The small discrepancy between the measured and tabulated values can be related to omitting the radial displacement correction [7]. Essentially the same can be said about hardness, for which a reference value of 8.0 GPa is normally used. In this context, the other 2 types of borosilicate glasses are relatively far from the typical values for BK7 optical glass. Both BG33 and Simax glass exhibit lower hardness and reduced modulus, with the lowest hardness values observed for Simax. Significant differences between BK7 and the other two glasses are also observed in the value of the so-called Plasticity Index which is the ratio between plastic and total deformation (W_p/W_t) calculated from the areas defined by the load-displacement curve. BK7 glass exhibits a higher extent of plastic deformation (~45%) compared to BG33 and Simax glass (~36%).

Nanoindentation carried out at higher loads of 100 and 250, and 500 mN was used for the exploration of crack formation susceptibility. The records of AE signal reveal lower/zero AE activity in the case of the samples prepared by hand machining (see Fig. 2(a, b)). It should be emphasized that the AE activity was only observed during loading. This can be assigned to the formation of medial cracks in accordance with the theory [2]. The trend of AE activity of these samples decreases in the order of BK7 to BG33 to Simax. The different behavior of hand- and CNC-machined surfaces can be linked to different subsurface damage caused by different contact conditions between the workpiece and the instrument/abrasive. As a result, a different density of surface and especially (near)-subsurface flaws are present in the glass. These flaws, typically represented by pre-cracks, act as sources for AE activity during their growth when elastic energy is suddenly released. To quantify the AE activity, the individual hits representing individual cracking events can be analyzed. Fig. 2(c) clearly shows that the total energy detected by the AE system, calculated as a sum for all hits, is always substantially higher for CNC machined glasses and increases with the applied normal load during indentation. Similar trends are observed for the total number of hits, see Fig. 2(d).

The confocal microscope images of the residual impressions and SEM images (see Fig. 3) did not prove any cracking on the surface around the impression. This implies that AE allows the detection of the formation of subsurface cracks.

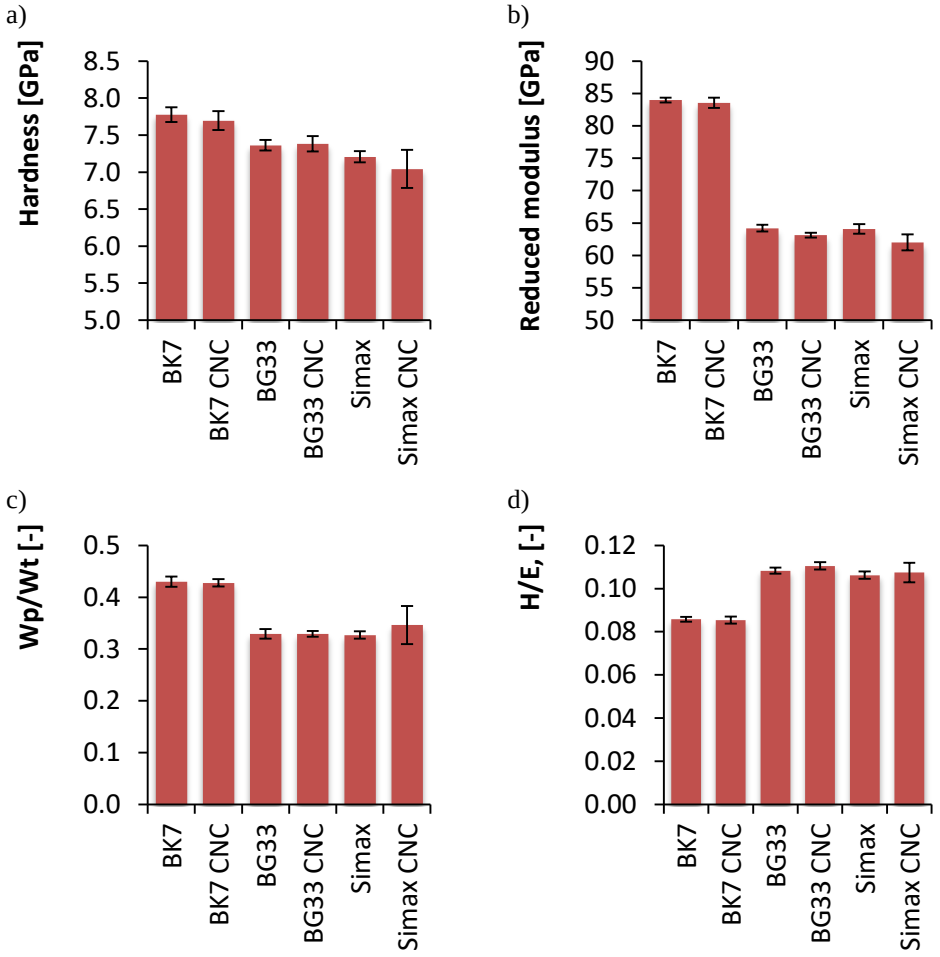

Fig. 1. Nanoindentation results for 10 mN tests and time schedule 10-10-10 s: a) indentation hardness, b) indentation reduced modulus, c) plasticity index (W_p/W_t), d) ratio of H/E.

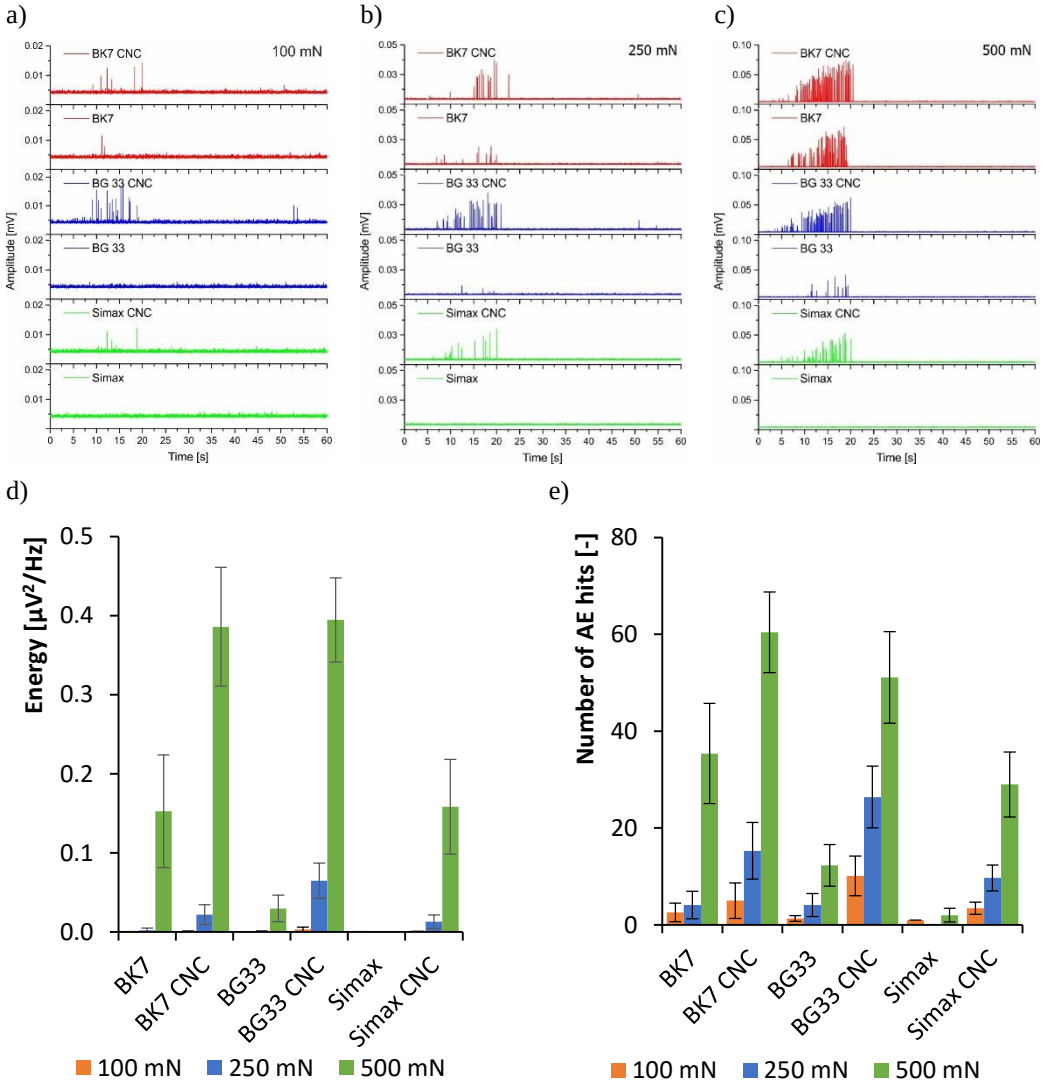

Fig. 2. Acoustic emission records for nanoindentation: a) AE envelope for 100 mN, b) AE envelope for 250 mN, c) AE envelope for 500 mN,d) the total energy of AE hits and e) the total numbers of AE hits at 100, 250, and 500 mN.

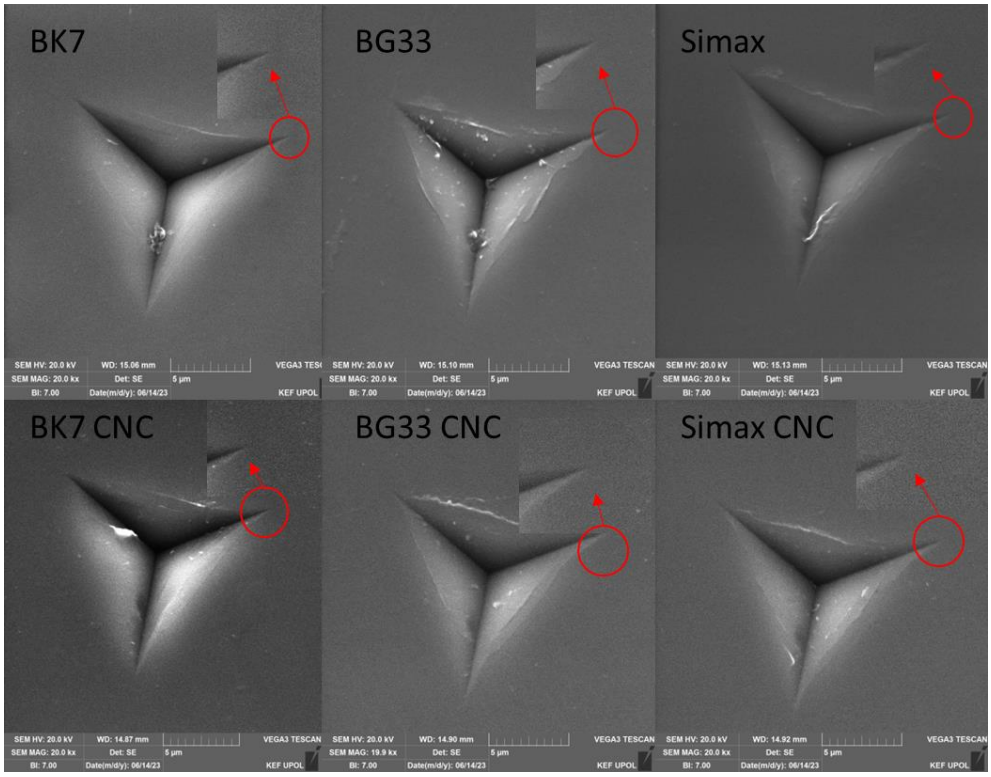

Fig. 3. SEM images of residual indents for a load of 500 mN.

Microindentation induced cracking

To quantify indentation cracking, the length of the radial crack emanating from the apex of a triangular indentation formed at relatively large normal forces of 1, 5, 10, and 20 N was measured. The longest radial cracks were observed for BK7 glass regardless of the maximum normal load applied during indentation, see the comparison in Fig. 4. This suggests that BK7 glass is visually more prone to cracking which is a sign of lower toughness (higher brittleness), as can be seen in the overview image in Fig. 5. It should be noted that application of higher load substantially changed the deformation response as cracking under the indenter occurred, compare Fig. 3 and Fig. 5.

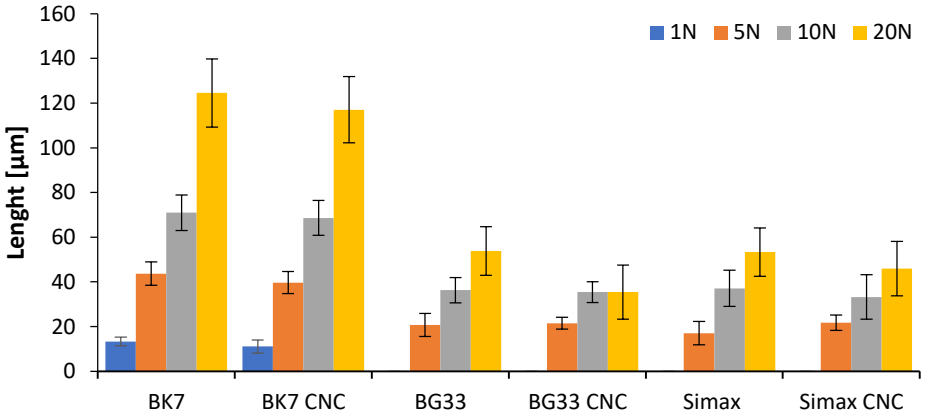

Fig. 4. Length of the radial cracks emanating from the apex of a triangular indentation with Berkovich indenter.

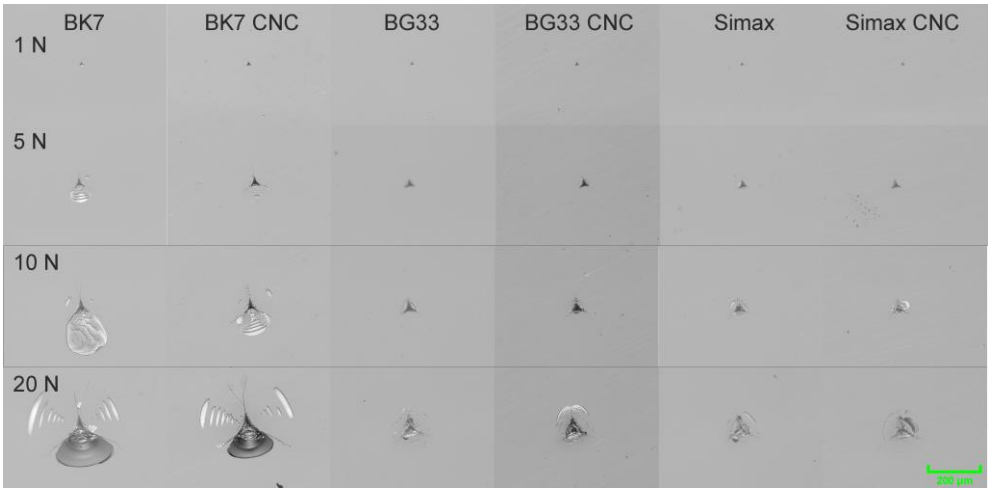

Fig. 5. Images of the residual indents formed on the surface of indented borosilicate glasses.

Visual comparison of AE envelopes obtained for indentations up to different loads is shown in Fig. 5(a, b) where only data for 1 and 5 N are presented. For easier comparison, the AE records were analyzed at the level of individual AE hits, and various parameters were evaluated such as the total number of hits, and total cumulative hit energy, see Fig. 5(c, d). From the number of hits, BK7 glass has the lowest number of total detected AE events, while the total cumulative hit energy is comparable to other glasses for tests performed at 1, 5, and 10 N. However, a further increase of indentation load to 20 N led to a substantial change in AE response. For BK7 these tests performed at 20N a significantly higher total cumulative hit energy was observed, which reflects a strong cracking in the vicinity of the indenter. It should be noted that the AE signal was observed mainly during loading when the indenter was penetrating the surface, but also during unloading and as well during relaxation when the surface was completely unloaded. The distribution of AE peaks on the AE envelope reflects the extent and type of different crack types evolving

during loading and unloading. While median cracks are formed during loading when the indenter is penetrating the sample surface, the lateral cracks grow when stress is released during unloading [8] The character of crack patterns correlates well with the AE detection(compare Fig. 5 and Fig. 6).

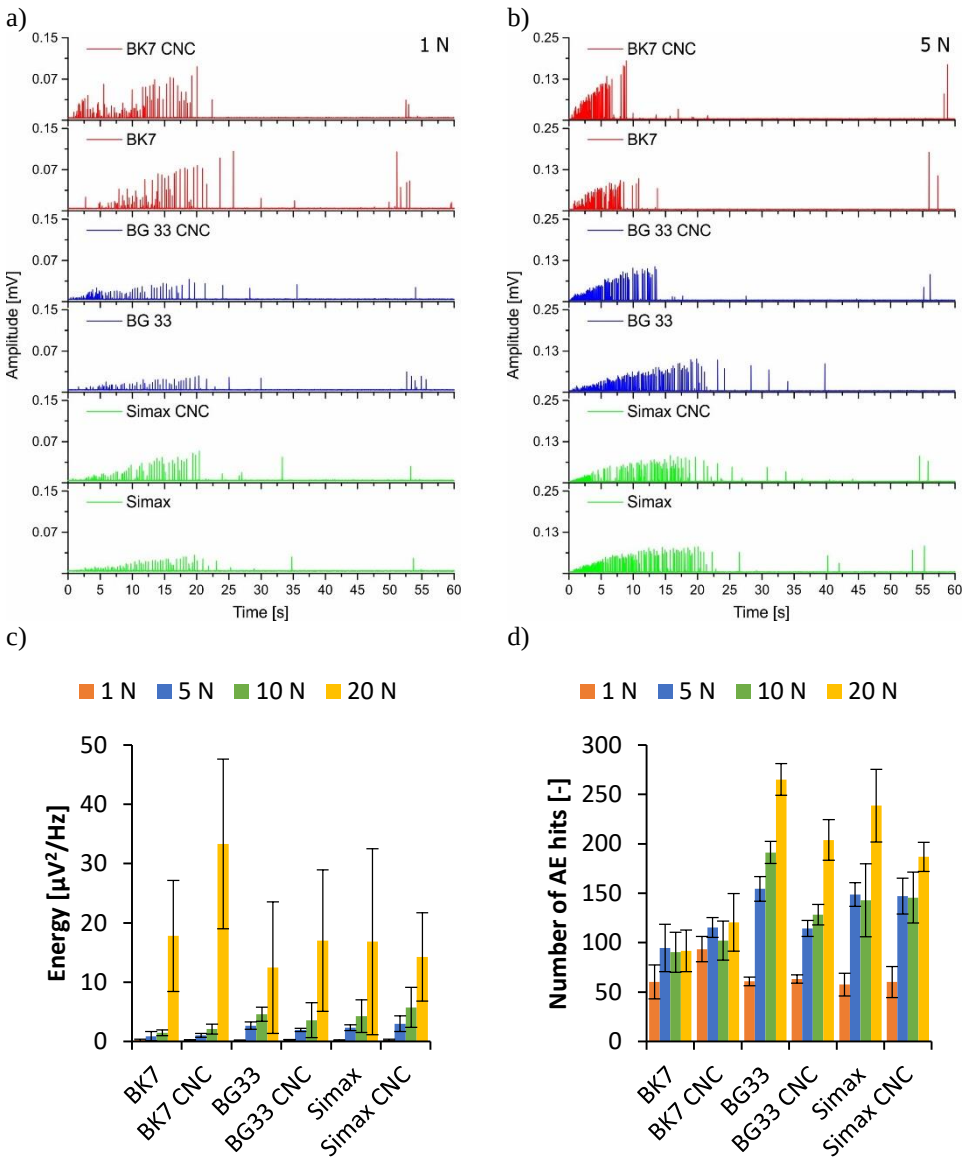

Fig. 6. A) Acoustic emission; b) typical AE envelopes for indentation performed up to 1 and 5 N; c) total cumulative AE hit energy; d) the total number of AE hits.

Dynamic impulse test

Analysis of the impact penetration depth record revealed small differences in the initial depths of the very first contact conducted in the quasistatic regime, see Fig. 7. The lowest value was recognized for the BK7 samples, both hand and machine-treated, which is consistent with their highest hardness values. Interestingly, the penetration depth for the subsequent 1st dynamic impact is similar for all samples, regardless of the type of machining. The value of the final penetration depth after 70 impacts is comparable for BG33 and Simax, while for BK7-CNC it reaches almost two times higher value. This difference in BK7 glass compared to the other glasses can be related to its higher hardness and lower resistance to crack formation/propagation. This higher "brittleness" is manifested in the residual craters/indents. Based on the lowest final penetration depth, the best resistance to repeated dynamic impact was identified for BG33 glass. It should be noted that the 1st impact penetration depth reached slightly shallower depths.

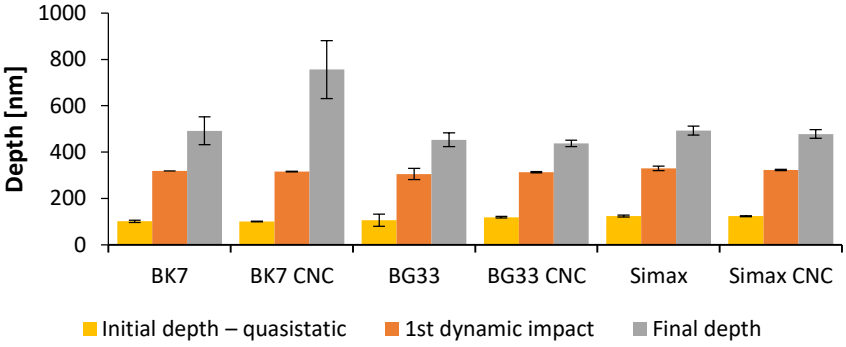

Fig. 7. Comparison of characteristic penetration depths detected during the dynamic impact test.

A comparison in terms of AE activity in Fig. 7 shows that the BK7 glass samples possess the highest AE amplitude, the highest cumulative total energy as well as the number of AE hits. This is in good agreement with the visual observation of the residual craters with pronounced cracking and material loss via chipping (see BK7 on Fig. 8(c))

AE envelopes for BG33 and Simax are almost overlapping for CNC machined samples in contrast to manually machined samples, where Simax glass exhibits lower values of cumulative total AE hit energy, as well as the AE hit number. This behavior can be attributed to the lower surface finish quality of the CNC machining. In other words, the presence of subsurface cracks from CNC machining does not allow us to distinguish between these glasses.

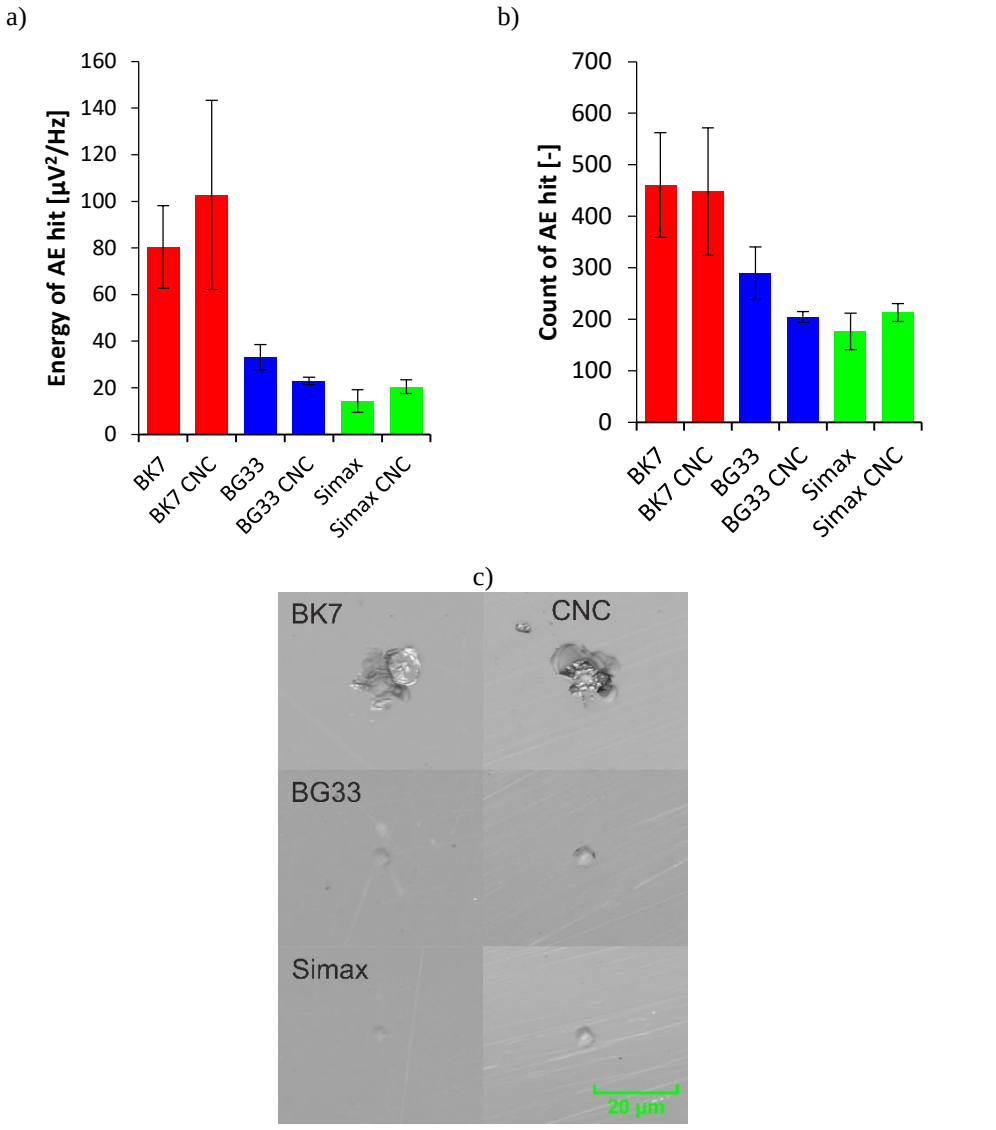

Fig. 8. Results of AE signal evaluation for a dynamic impact test a) a) cumulative total AE hit energy, b) the total number of AE hits, and c) images of the residual craters formed after impulse test on the surface of borosilicate glasses.

CONCLUSIONS

Depth sensing indentation and dynamic impact test coupled with AE detection were used for the exploration of the mechanical durability of three different types of borosilicate glasses machined manually and using a CNC machine. Nanoindentation points out that BK7 glass, which is an optical grade glass, exhibits higher hardness and reduced modulus compared to Simax and BG33 glass considered industrial-grade glass. Hardness and reduced modulus were comparable for BG33 and Simax reflecting their similar chemical composition. Simax is slightly softer than BG33 glass, which together with the less pronounced AE may indicate a lower amount of subsurface cracks. Analysis of AE signals detected during the nanomechanical testing proved to be very effective in distinguishing differences between the type of machining (manual vs CNC), with manually machined samples generally having lower amplitudes of AE signals or eventually no AE activity was detected. In the case of CNC machined glasses, probably the higher density of subsurface pre-cracks and voids leads to lower damage tolerance. These pre-cracks may initiate further crack growth/propagation under local mechanical stress and hence a more pronounced AE signal representing a sudden release of stored energy. This does not generally imply the lower surface quality of CNC machining but rather reflects different surface interactions between the machining instrument and the workpiece as well as time demands.

Analysis of the crack patterns and length of radial cracks around the residual indent formed during microindentation suggests very similar resistivity against crack formation in the case of industrial glass Simax and BG 33. BK7 glass has approximately 2,5 longer radial cracks compared to the other two glasses, so the resistance to crack initiation/ propagation is lower for BK7 than for industrial glasses BG33 and Simax. This is consistent with the results of resistance to repeated dynamic impact as BK7 glass shows significantly lower damage tolerance in comparison to BG33 and Simax glass as evidenced also via analysis of AE activity. For the test with a higher indentor load like microindentation or with repeated deformation like in the case of the dynamic test, we do not observe a significant difference in glass behavior depending on the type of machining.

In general, AE proved to be a very useful method for obtaining complementary and often unique information on the deformation response glasses during localized mechanical loading even at the nano/micro scale. But it should also be noted that in case of sufficiently high indentation load, AE no longer allows to distinguish differences between samples. The stress under the indenter is so high, corresponding to the rate of deformation, that the material response is manifested by continuous cracking.

ACKNOWLEDGMENT

The authors gratefully acknowledge the support by the Project TN01000038/11 of the Technology Agency of the Czech Republic and the Operational Programme Research, Development and Education, Projects Nos. CZ.02.1.01/0.0/0.0/17_049/0008422. This work was also supported by the project IGA_PrF_2023_005 of Palacky University.

REFERENCES

[1] Hasanuzzaman, M., Rafferty, A., Sajjia, M., Olabi, AG.: Reference Module in Materials Science and Materials Engineering, 2016
[2] Fischer-Cripps, A.C.: Nanoindentation, Springer New York, New York, 2004
[3] Lawn, BR.: J. Am. Ceram. Soc., vol. 81, no. 8, 1998, p. 1977-1994
[4] Ctvrtlik, R., Tomastik, J., Vaclavek, L. Beake, BD., Harris, AJ., Martin, AS., Hanak, M., Abrham, P.: JOM 71, 2019, p. 3358–3367

[5] Oliver, W.C., Pharr, G.M.: J. Mater. Res., vol. 7, 1992, p. 1564–1583
[6] Bach, H., Neuroth, N.: The properties of optical glass, Springer-Verlag Berlin, Heidelberg, 1998.
[7] Kovář, J., Fuis, V., Čtvrtlík, R., Tomáštík, J.: J. Mater. Res., vol. 37, 2022, p. 1750–1761.
[8] Lawn, BR., Evans, A.G., Marshall, J. Am. Ceram. Soc., vol. 63, no. 9-10: p. 574-581.